Regulation of immune receptor kinases plasma membrane nanoscale landscape by a plant peptide hormone and its receptors

Julien Gronnier[1,2,7], Christina M. Franck[1], Martin Stegmann[2,8], Thomas A. DeFalco[1,2], Alicia Abarca[1], Michelle Von Arx[1], Kai Dünser[3], Wenwei Lin[4], Zhenbiao Yang[4], Jürgen Kleine-Vehn[5,6], Christoph Ringli[1], and Cyril Zipfel[1,2]

[1]Institute of Plant and Microbial Biology and Zurich-Basel Plant Science Center, University of Zurich, 8008 Zurich, Switzerland.

[2]The Sainsbury Laboratory, University of East Anglia, Norwich Research Park, NR4 7UH, Norwich, UK.

[3]Department of Applied Genetics and Cell Biology, University of Natural Resources and Life Sciences Vienna, 1190 Vienna, Austria.

[4]FAFU-UCR Joint Center for Horticultural Biology and Metabolomics Center, Haixia, Institute of Science and Technology, Fujian Agriculture and Forestry University, Fuzhou, Fujian, China.

[5]Faculty of Biology, Department of Molecular Plant Physiology (MoPP), University of Freiburg, 79104 Freiburg, Germany.

[6]Center for Integrative Biological Signalling Studies (CIBSS), University of Freiburg, 79104 Freiburg, Germany.

[7]Present address: University of Tübingen, Center for Plant Molecular Biology (ZMBP), 72076 Tübingen, Germany.

[8]Present address: Phytopathology, School of Life Sciences Weihenstephan, Technical University of Munich, Freising, Germany.

Correspondence: Cyril Zipfel, cyril.zipfel@botinst.uzh.ch

ABSTRACT

Spatial partitioning is a propensity of biological systems orchestrating cell activities in space and time. The dynamic regulation of plasma membrane nano-environments has recently emerged as a key fundamental aspect of plant signaling, but the molecular components governing it are still mostly unclear. The receptor kinase FERONIA (FER) controls complex formation of the immune receptor kinase FLAGELLIN SENSING 2 (FLS2) with its co-receptor BRASSINOSTEROID INSENSITIVE 1-ASSOCIATED KINASE 1 (BAK1), and this function is inhibited by the FER ligand RAPID ALKALANIZATION FACTOR 23 (RALF23). Here, we show that FER regulates the plasma membrane nanoscale organization of FLS2 and BAK1. Our study demonstrates that akin to FER, leucine-rich repeat (LRR) extensin (LRXs) proteins contribute to RALF23 responsiveness, regulate BAK1 nanoscale organization and immune signaling. Furthermore, RALF23 perception leads to rapid modulation of FLS2 and BAK1 nanoscale organization and its inhibitory activity on immune signaling relies on FER kinase activity. Our results suggest that perception of RALF peptides by FER and LRXs actively modulates the plasma membrane nanoscale landscape to regulate cell surface signaling by other receptor kinases.

INTRODUCTION

Multicellular organisms evolved sophisticated surveillance systems to monitor changes in their environment. In plants, receptor kinases (RKs) and receptor proteins (RPs) are the main ligand-binding cell-surface receptors perceiving self, non-self, and modified-self molecules (Hohmann, Lau and Hothorn, 2017). For example, recognition of pathogen-associated molecular patterns (PAMPs) by pattern recognition receptors (PRRs) initiates signaling events leading to PRR-triggered immunity (PTI) (Couto and Zipfel, 2016; Yu *et al.*, 2017). The *Arabidopsis thaliana* (hereafter Arabidopsis) leucine-rich repeat receptor kinases (LRR-RKs) FLAGELLIN SENSING 2 (FLS2) and EF-TU RECEPTOR (EFR) recognize the bacterial PAMPs flagellin (or its derived epitope flg22) and elongation factor-Tu (or its derived epitope elf18), respectively (Gómez-Gómez and Boller, 2000; Zipfel *et al.*, 2006). Both FLS2 and EFR form ligand-induced complexes with the co-receptor LRR-RK BRASSINOSTEROID INSENSITIVE 1-ASSOCIATED KINASE 1/SOMATIC EMBRYOGENESIS RECEPTOR KINASE 3 (BAK1/SERK3, hereafter BAK1) to initiate immune signaling, such as for instance, the production of apoplastic reactive oxygen species (ROS) (Chinchilla *et al.*, 2007; Schulze *et al.*, 2010; Schwessinger *et al.*, 2011; Sun *et al.*, 2013).

We previously showed that the *Catharanthus roseus* RECEPTOR-LIKE PROTEIN KINASE 1-LIKE (CrRLK1L) FERONIA (FER) and the LORELEI-LIKE-GPI ANCHORED PROTEIN 1 (LLG1) are required for flg22-induced FLS2-BAK1 complex formation (Stegmann *et al.*, 2017; Xiao *et al.*, 2019). Notably, the endogenous RAPID ALKALINIZATION FACTOR 23 (RALF23) is perceived by a LLG1-FER complex, which leads to inhibition of flg22-induced FLS2-BAK1 complex formation (Stegmann *et al.*, 2017; Xiao *et al.*, 2019). As such, although FER and LLG1 are positive regulator of PTI, RALF23 is a negative regulator. How these components regulate FLS2-BAK1 complex formation remains however unclear.

Members of the CrLKL1s family are involved in RALF perception (Ge *et al.*, 2017; Gonneau *et al.*, 2018; Liu *et al.*, 2021). Among them, FER plays a pivotal role in the perception of several Arabidopsis RALF peptides (Haruta *et al.*, 2014; Stegmann *et al.*, 2017; Gonneau *et al.*, 2018; Zhao *et al.*, 2018; Abarca, Franck and Zipfel, 2021; Liu *et al.*, 2021). In addition, cell-wall associated LEUCINE RICH REPEAT-EXTENSINs (LRXs) proteins are also involved in CrRLK1L-regulated pathways and were shown to be high-affinity RALF-binding proteins (Mecchia *et al.*, 2017; Zhao *et al.*, 2018; Dünser *et al.*, 2019; Moussu *et al.*, 2020). Structural and biochemical analyses have shown that RALF-binding by CrRLK1L/LLGs complexes and LRXs are mutually exclusive and mechanistically distinct from each other (Xiao *et al.*, 2019; Moussu *et al.*, 2020). While CrRLK1Ls and LRXs have emerged as important RALF-regulated signaling modules, it is still unknown whether LRXs are also involved in RALF23-mediated regulation of immune signaling.

76 Plasma membrane lipids and proteins dynamically organize into diverse membrane
77 domains giving rise to fluid molecular patchworks (Gronnier *et al.*, 2018; Jaillais and Ott, 2020).
78 These domains are proposed to provide dedicated biochemical and biophysical environments
79 to ensure acute, specific and robust signaling events (Gronnier *et al.*, 2019; Jacobson, Liu and
80 Lagerholm, 2019). For instance, FLS2 localizes in discrete and static structures proposed to
81 specify immune signaling (Bücherl *et al.*, 2017). The cell wall is thought to impose physical
82 constraints on the plasma membrane, limiting the diffusion of its constituents (Feraru *et al.*,
83 2011; Martinière *et al.*, 2012). Indeed, alteration of cell wall integrity leads to aberrant protein
84 motions at the plasma membrane (Martinière *et al.*, 2012; McKenna *et al.*, 2019). Notably,
85 perturbation of the cell wall affects FLS2 nanoscale organization (McKenna *et al.*, 2019).
86 Despite its imminent importance, it remains largely unknown how the cell wall and its integrity
87 modulate the organization of the plasma membrane. Interestingly, both CrRLK1Ls and LRXs
88 are proposed cell wall integrity sensors and conserved modules regulating growth,
89 reproduction and immunity (Franck, Westermann and Boisson-Dernier, 2018; Herger *et al.*,
90 2019). However, their mode of action and potential link to RALF perception, are still poorly
91 understood.
92 Here, we show that FER regulates the plasma membrane nanoscale organization of
93 FLS2 and BAK1. Similarly, we show that LRXs contribute to RALF23 responsiveness, regulate
94 BAK1 nanoscale organization and immune signaling. Importantly, our work reveals an
95 unexpected uncoupling of FER and LRXs modes-of-action in growth and immunity. We
96 demonstrate that RALF23 perception leads to rapid modulation of FLS2 and BAK1 nanoscale
97 organization and that its inhibitory activity on immune signaling requires FER kinase activity.
98 We propose that the regulation of the plasma membrane nanoscale organization by RALF23
99 receptors underscores their role in the formation of protein complexes and initiation of immune
100 signaling.
101
102 **RESULTS AND DISCUSSION**

103 **FER regulates membrane nanoscale organization of FLS2 and BAK1**
104 We combined variable angle total internal reflection fluorescence microscopy (VA-TIRFM) and
105 single-particle tracking to analyze the lateral mobility of FLS2-GFP proteins in transgenic
106 Arabidopsis lines. Two lines expressing FLS2-GFP under the control of its native promoter
107 were crossed with two *FER* knock-out alleles, *fer-2* and *fer-4*. In line with previous reports
108 (Bücherl *et al.*, 2017; Tran *et al.*, 2020), we observed that FLS2-GFP localizes to static foci in
109 the wild-type (WT) (Movie S1). Consistently, FLS2-GFP single particle trajectories exhibit a
110 confined mobility behavior (Fig. S1, Movie S1). Comparative analysis of the diffusion
111 coefficient (D), which describes the diffusion properties of detected single particles, showed
112 that FLS2-GFP is more mobile in *fer* mutants than in WT (Fig. S1, S2 and Movie S1). To

113 analyze FLS2-GFP organization, we reconstructed images using a temporal averaging of
114 FLS2-GFP fluorescence observed across VA-TIRFM time series. Furthermore, individual
115 image sections were subjected to kymograph analysis. Using this approach, we found that
116 FLS2-GFP fluorescence is maintained into well-defined and static structures in WT, while it
117 appears more disperse and more labile in both *fer* mutants (Fig. 1A-B and S2). To substantiate
118 these observations, we used previously established spatial clustering index (SCI) which
119 describes protein lateral organization (Gronnier *et al.*, 2017; Tran *et al.*, 2020). As expected,
120 SCI of FLS2-GFP was lower in *fer-4* than in WT (Fig. 1C), indicating disturbance in FLS2-GFP
121 lateral organization.
122 In *Medicago truncatula* and in yeast, alteration of nanodomain localization has been linked to
123 impaired protein accumulation at the plasma membrane due to increased protein endocytosis
124 (Grossmann *et al.*, 2008; Liang *et al.*, 2018). To inquire for a potential defect in FLS2 plasma
125 membrane accumulation, we observed sub-cellular localization of FLS2-GFP using confocal
126 microscopy. The analysis revealed a decrease in FLS2-GFP accumulation in *fer* mutants (Fig.
127 S3). Altogether, these results show that *FER* is genetically required to control FLS2-GFP
128 nanoscale organization and accumulation at the plasma membrane.
129 To further characterize the impact of *FER* loss-of-function in RK organization, we analyzed the
130 behavior of BAK1-mCherry at the plasma membrane. Fluorescence recovery after
131 photobleaching experiments previously suggested that the vast majority of BAK1 molecules
132 are mobile (Hutten *et al.*, 2017). Consistent with this result, BAK1-mCherry was much more
133 mobile than FLS2-GFP in the WT background (Sup Movie 2). Given that BAK1 is a common
134 co-receptor for multiple LRR-RK signaling pathways, we hypothesize that BAK1 might
135 dynamically associates with various pre-formed signaling platforms, such as FLS2
136 nanodomains (Fig. 1, (Bücherl *et al.*, 2017)). Under our experimental conditions, we were not
137 able to perform high-quality single particle tracking analysis for BAK1-mCherry (Sup Movie 2,
138 see methods section). However, visual inspection of particles behavior suggests that BAK1-
139 mCherry is less mobile in *fer-4* than in WT (Sup Movie 2). In good agreement, reconstructed
140 VA-TIRFM images and kymographs show that BAK1-mCherry fluorescence is more structured
141 and static in *fer-4* than in WT (Fig. 1F). Furthermore, we observed an increase of BAK1-
142 mCherry SCI in *fer-4* (Fig 1G). Confocal microscopy analysis did not reveal significant
143 differences in BAK1-mCherry plasma membrane accumulation between *fer-4* and WT
144 backgrounds (Fig. S4). Altogether, these data show that loss of *FER* perturbs FLS2 and BAK1
145 nanoscale organization, albeit in an opposite manner (Fig. 1D and H). Previous reports have
146 similarly shown that altering the composition of the cell wall can lead to opposed effects on the
147 mobility of different proteins. For instance, inhibition of cellulose synthesis increases the
148 mobility of HYPERSENSITIVE INDUCED REACTION 1 (HIR1) (Daněk *et al.*, 2020) but limits
149 the mobility of LOW TEMPERATURE INDUCED PROTEIN 6B (Lti6b) (Martinière *et al.*, 2012;

150 Daněk *et al.*, 2020). Modification of pectin methyl esterification status increases the mobility of
151 FLS2 (McKenna *et al.*, 2019) but decreases the mobility of FLOTILIN 2 (FLOT2) (Daněk *et al.*,
152 2020). Collectively, these observations suggest that various membrane environments are
153 differentially regulated by the cell wall and the proposed cell wall integrity sensor FER.
154
155 **LRX3, LRX4 and LRX5 regulate BAK1 nanoscale organization and PTI signaling**
156 LRXs are dimeric, cell wall-localized, high-affinity RALF-binding proteins suggested to monitor
157 cell wall integrity in growth and reproduction (Baumberger, Ringli and Keller, 2001; Mecchia *et*
158 *al.*, 2017; Dünser *et al.*, 2019; Herger *et al.*, 2019, 2020; Moussu *et al.*, 2020). Their extensin
159 domain confers cell wall anchoring while their LRR domain mediates RALF binding (Herger *et*
160 *al.*, 2019; Moussu *et al.*, 2020). Among the Arabidopsis 11-member *LRX* family, *LRX3*, *LRX4*,
161 and *LRX5* are the most expressed in vegetative tissues, and the *lrx3 lrx4 lrx5* triple mutant
162 (hereafter *lrx3/4/5*) shows stunted growth and salt hypersensitivity phenotypes reminiscent of
163 the *fer-4* mutant (Zhao *et al.*, 2018; Dünser *et al.*, 2019). Therefore, we hypothesized that LRXs
164 also regulate immune signaling. Indeed, our co-immunoprecipitation experiments showed that
165 *lrx3/4/5* is defective in flg22-induced FLS2-BAK1 complex formation (Fig. 2A). Consistently,
166 flg22-induced ROS production was reduced in *lrx3/4/5* similar to the levels observed in *fer-4*
167 (Fig. 2B). In addition, we found that *lrx3/4/5* was impaired in elf18-induced ROS production
168 (Fig. 2C), suggesting that, as for FLS2-BAK1 complex formation, *LRX3/4/5* are required for
169 complex formation between EFR and BAK1. Thus, we conclude that LRX3/4/5 are positive
170 regulators of PTI signaling.
171 We then asked whether, similar to FER, LRX3/4/5 regulate plasma membrane nanoscale
172 organization. We crossed lines expressing FLS2-GFP and BAK1-mCherry under the control of
173 their respective native promoter with *lrx3/4/5* background. However, despite several attempts,
174 we could not retrieve homozygous *lrx3/4/5* lines expressing FLS2-GFP. Nonetheless, VA-
175 TIRFM and confocal imaging showed that, like in *fer-4*, BAK1-mCherry is more organized and
176 more static in *lrx3/4/5* (Fig. 2D-E, Sup Movie 3), and that BAK1-mCherry plasma membrane
177 localization is not affected by the loss of *LRX3/4/5* (Fig. S4). Thus, like in *fer* mutants,
178 perturbation in PTI signaling observed in *lrx3/4/5* correlates with alterations of plasma
179 membrane RK organization.
180 Formerly, LRX3, LRX4 and LRX5 have been proposed to sequester RALF peptides to prevent
181 internalization of FER and inhibition of its function (Zhao *et al.*, 2018). Following this logic,
182 defects in PTI observed in *lrx3/4/5* could be explained by a depletion of FER at the plasma
183 membrane. However, our confocal microscopy analysis and western blotting with anti-FER
184 antibodies indicated that FER accumulation and plasma membrane localization is not affected
185 in *lrx3/4/5* (Fig. S5). Furthermore, VA-TIRFM revealed that FER-GFP transiently accumulates
186 in dynamic foci, independently of *LRX3/4/5* (Fig. S6, Sup movie 4). Together, these results

187 suggest that LRX3/4/5 do not prevent RALF association with FER to modulate PTI. Moreover,
188 our results suggest that active monitoring by the proposed cell wall integrity sensors FER and
189 LRXs regulates plasma membrane nanoscale dynamics of RKs.
190 The ability of LRX3/4/5 to associate with RALF23 *in planta* (Zhao *et al.*, 2018) prompted us to
191 test if LRX3/4/5 are required for RALF23 responsiveness. Indeed, *LRX3, LRX4* and *LRX5* were
192 required for RALF23-induced inhibition of ROS production upon elf18 treatment (Fig. S7A).
193 Similarly, we observed a decrease in the inhibition of seedlings growth triggered by RALF23
194 in *lrx3/4/5* compared to WT (Fig. S7B). Altogether, these data show that LRX3/4/5 contribute
195 to RALF23 responsiveness (Fig. S7C), and that LRXs and FER have analogous functions in
196 regulating PTI.
197 We next asked if FER and LRX3/4/5 form a complex. For this, we made use of a deleted
198 version of LRX4 lacking its extensin domain (LRX4$^{\Delta E}$), previously used to assess protein
199 complex formation (Dünser *et al.*, 2019; Herger *et al.*, 2020). Consistent with previous reports
200 on transient expression assays, (Dünser *et al.*, 2019; Herger *et al.*, 2020), co-
201 immunoprecipitation experiments with stably transgenic Arabidopsis showed that FER
202 associates constitutively with LRX4$^{\Delta E}$-FLAG, and that RALF23 treatment does not modulate
203 this association (Fig. S8). This suggests that FER-LRX complex-mediated direct monitoring of
204 the cell wall (Dünser *et al.*, 2019; Herger *et al.*, 2019) is not regulated by RALF23. In agreement
205 with structural and biochemical analyses of RALF-binding by CrRLK1L/LLGs and LRXs
206 (Moussu *et al.*, 2020), FER-LLG1 and LRX3/4/5 may form distinct RALF23 receptor
207 complexes. As in the cases of pollen tube and root hair growth and integrity (Ge *et al.*, 2017;
208 Mecchia *et al.*, 2017; Moussu *et al.*, 2020; Dünser *et al.*, 2019; Herger *et al.*, 2020), future
209 investigations are thus needed to understand the exact molecular link between RALF-binding
210 LRXs and CrRLK1s.
211
212 **Functional dichotomy of FER and LRXs in regulating growth and immunity**
213 In line with previous reports our data shows that FER and LRXs can form a complex ((Dünser
214 *et al.*, 2019; Herger *et al.*, 2019), Fig. S8). Moreover, they are known to associate with the cell
215 wall (Baumberger, Ringli and Keller, 2001; Feng *et al.*, 2018), and are proposed to relay co-
216 jointly its properties (Dünser *et al.*, 2019; Herger *et al.*, 2019). We thus asked if direct cell wall
217 sensing underlies FER and LRXs function in PTI. In the context of growth and cell expansion,
218 plants overexpressing LRX4$^{\Delta E}$, a truncated version of LRX4, are phenotypically reminiscent of
219 *lrx3/4/5* triple mutants and the *fer-4* single mutant (Dünser *et al.*, 2019). This dominant negative
220 effect is proposed to be caused by competition of the overexpressed truncated LRX4$^{\Delta E}$ with
221 endogenous LRXs and consequent loss of cell wall anchoring (Dünser *et al.*, 2019). Similarly,
222 overexpression of LRX1$^{\Delta E}$ inhibits root hair elongation, phenocopying loss of function of *LRX1*
223 and *LRX2* (Herger *et al.*, 2020). By contrast, we observed that LRX4$^{\Delta E}$ does not affect flg22-

224 induced interaction between FLS2 and BAK1 (Fig. S9A). In good agreement with this notion,
225 overexpression of LRX4$^{\Delta E}$ did not affect flg22 nor elf18-induced ROS production (Fig. S9B-C).
226 To corroborate these results, we tested inhibition of root growth triggered by flg22 treatment.
227 Consistent with the positive role of FER and LRX3/4/5 in PTI, we observed that *fer-4* and
228 *lrx3/4/5* are hyposensitive to flg22 treatment (Fig S9D). By contrast, overexpression of LRX4$^{\Delta E}$
229 did not affect inhibition of root growth by flg22 (Fig S9D). In addition, we observed that LRX4$^{\Delta E}$
230 does not impact RALF23 responsiveness (Fig S9E). Altogether, these data suggest that the
231 function of LRX3/4/5 in PTI is distinct from their role during growth.
232 The ectodomain of FER contains two malectin-like domains, malA and malB (Fig 3A), which
233 share homology with malectin, a carbohydrate-binding protein from *Xenopus laevis* (Boisson-
234 Dernier, Kessler and Grossniklaus, 2011). Despite lacking the canonical carbohydrate-binding
235 site of malectin (Moussu *et al.*, 2018; Xiao *et al.*, 2019), malA and malB have been proposed
236 to bind pectin *in vitro* (Feng *et al.*, 2018) and FER-mediated cell wall-sensing regulates
237 morphogenesis (Duan *et al.*, 2010; Lin *et al.*, 2018). To investigate if direct cell wall-sensing
238 underlies FER`s function in regulating PTI, we used transgenic lines expressing a FER
239 truncated mutant lacking the malA-domain C-terminally fused to YFP (FER$^{\Delta malA}$-YFP) in the
240 *fer-4* mutant background (Fig 3B). We observed that FER$^{\Delta malA}$-YFP did not complement cell
241 shape or root hair elongation defect of *fer-4* (Fig. 3C-D), emphasizing the importance of malA
242 in FER-regulated cell morphogenesis. In contrast, immuno-precipitation assays showed that
243 FER$^{\Delta malA}$-YFP fully complements flg22-induced complex formation between endogenous FLS2
244 and BAK1 (Fig. 3E) as well as ROS production in response to flg22 and elf18 (Fig. 3F-G).
245 Altogether, these data suggest that malA-mediated cell wall sensing underlies specific
246 function(s) of FER in regulating growth and cell morphology, but is dispensable for FER´s role
247 in PTI. Interestingly, we observed that expression of FER$^{\Delta malA}$-YFP restores inhibition of growth
248 triggered by RALF23, suggesting that malB is sufficient for RALF responsiveness (Fig. 3H), as
249 suggested by its physical interaction with RALF23 (Xiao *et al.*, 2019). While we cannot formally
250 exclude the implication of pectin-binding by malB in regulating immunity, the contrasted
251 context-dependent functionality of FER$^{\Delta malA}$-YFP suggests that FER´s function in PTI is
252 primarily mediated by RALF perception. Altogether, our data indicate molecular and functional
253 dichotomy of FER and LRXs in regulating growth and immunity.
254
255 **RALF23 alters FLS2 and BAK1 organization and function through active FER signaling.**
256 We next asked if RALF23 activity is mediated by active FER signaling. We used a kinase-dead
257 mutant, FER^{K565R} C-terminally fused to GFP, expressed in *fer* knock-out backgrounds and
258 selected lines accumulating it to level similar to endogenous FER in WT background (Fig. S10;
259 Fig S11 (Chakravorty, Yu and Assmann, 2018)). Interestingly, we observed that FER^{K565R}-GFP
260 complements *fer*'s defect in FLS2-BAK1 complex formation (Fig. S10A) and PAMP-induced

261 ROS production (Fig. S10B-C). In contrast, we observed that inhibition of FLS2-BAK1 complex
262 formation by RALF23 depends on FER kinase activity (Fig. S11B. Similarly, inhibition of elf18-
263 induced ROS production and seedlings growth inhibition by RALF23 depended on FER kinase
264 activity (Fig. S11C). Overall, these data show that inhibition by RALF23 is mediated by active
265 FER signaling while FER's positive role in immune signaling is kinase activity-independent.
266 We next asked if inhibition of FLS2-BAK1 complex formation by RALF23 correlates with a
267 modulation of FLS2 or BAK1 nanoscale organization. VA-TIRFM imaging showed an increase
268 of FLS2-GFP mobility and an alteration of FLS2-GFP nanodomain organization within minutes
269 of RALF23 treatment (Fig. S12 and S13, Movie S7, imaging performed 2 to 30 min post-
270 treatment Fig. S14). Similarly, we observed that RALF23 treatment affects BAK1-mCherry
271 nanoscale organization (Fig. 5, Fig. S14, Movie S2). These data suggest that RALF23
272 perception leads to rapid modification of FLS2 and BAK1 membrane organization and thereby
273 potentially inhibits their association. It will be important in the future to identify the components
274 mediating RALF23 signaling and modification of FLS2 and BAK1 nanoscale dynamics.
275 In sum, our study unravels the regulation of FLS2 and BAK1 nanoscale organization by the
276 RALF receptors FER and LRX3/4/5. The function of RALF receptors in other processes might
277 similarly rely on the regulation of RK nanoscale dynamics, and the identification of the
278 corresponding regulated RKs is an exciting prospect for future investigation.
279

280 **ACKNOWLEDGMENTS**

281 We thank all present and past members of the Zipfel laboratory for fruitful discussions and
282 comments on the manuscript. We thank the members of the Grossniklaus, Ringli, Sanchez-
283 Rodriguez and Keller laboratories for sharing results and comments during our stimulating
284 CCWI meetings. We thank Vera Gorelova, Yvon Jaillais and Birgirt Kemmerling for comments
285 on the manuscript. This research was funded by the Gatsby Charitable Foundation (C.Z.), the
286 University of Zürich (C.Z.), the European Research Council under the Grant Agreements
287 309858 and 773153 (grants PHOSPHinnATE and IMMUNO-PEPTALK to C.Z.) and 639678
288 (grant AuxinER to J.K-V), the Swiss National Science Foundation (grant no. 31003A_182625
289 to C.Z. and 31003A_166577/1 to C.R.), and the Austrian science fund (FWF; P 33044 to J.K-
290 V). J.G., C.M.F. and T.A.D. were supported by Long-Term Fellowships from the European
291 Molecular Biology Organization (EMBO) (numbers 438-2018, 512-2019 and 100-2017,
292 respectively), while M.S. was supported by a post-doctoral fellowship (STE 2448/1) from the
293 Deutsche Forschungsgemeinschaft (DFG) and K.D. by a doctoral fellowship from the Austrian
294 Academy of Sciences (ÖAW). We thank Dr. Sarah Assman for providing segregating lines of
295 *fer-4*/pFER::FER^{K565R}-GFP, Prof. Sacco de Vries for kindly providing Col-0/pBAK1::BAK1-
296 mCherry line and Dr. Silke Robatzek for Col-0/pFLS2::FLS2-GFP lines, and Dr. Nana Keinath
297 for kindly offering *fer-2*/pFER::FER^{K565R}-GFP lines.

298

299 **REFERENCES**

300

301 Abarca, A., Franck, C. M. and Zipfel, C. (2021) 'Family-wide evaluation of RAPID
302 ALKALINIZATION FACTOR peptides', *Plant Physiology*. doi: 10.1093/PLPHYS/KIAB308.

303 Baumberger, N., Ringli, C. and Keller, B. (2001) 'The chimeric leucine-rich repeat/extensin
304 cell wall protein LRX1 is required for root hair morphogenesis in Arabidopsis thaliana', *Genes*
305 *and Development*, 15(9), pp. 1128–1139. doi: 10.1101/gad.200201.

306 Boisson-Dernier, A., Kessler, S. A. and Grossniklaus, U. (2011) 'The walls have ears: The
307 role of plant CrRLK1Ls in sensing and transducing extracellular signals', *Journal of*
308 *Experimental Botany*, pp. 1581–1591. doi: 10.1093/jxb/erq445.

309 Bücherl, C. A. *et al.* (2013) 'Visualization of BRI1 and BAK1(SERK3) Membrane Receptor
310 Heterooligomers during Brassinosteroid Signaling', *Plant Physiology*, 162(4), p. 1911. doi:
311 10.1104/PP.113.220152.

312 Bücherl, C. A. *et al.* (2017) 'Plant immune and growth receptors share common signalling
313 components but localise to distinct plasma membrane nanodomains', *eLife*, 6. doi:
314 10.7554/eLife.25114.

315 Chakravorty, D., Yu, Y. and Assmann, S. M. (2018) 'A kinase-dead version of FERONIA
316 receptor-like kinase has dose-dependent impacts on rosette morphology and RALF1-
317 mediated stomatal movements', *FEBS Letters*, 592(20), pp. 3429–3437. doi: 10.1002/1873-
318 3468.13249.

319 Chinchilla, D. *et al.* (2007) 'A flagellin-induced complex of the receptor FLS2 and BAK1
320 initiates plant defence', *Nature*, 448(7152), pp. 497–500. doi: 10.1038/nature05999.

321 Couto, D. and Zipfel, C. (2016) 'Regulation of pattern recognition receptor signalling in
322 plants', *Nature Reviews Immunology*, 16, pp. 537–552. doi: 10.1038/nri.2016.77.

323 Daněk, M. *et al.* (2020) 'Cell wall contributes to the stability of plasma membrane
324 nanodomain organization of *Arabidopsis thaliana* FLOTILLIN2 and HYPERSENSITIVE
325 INDUCED REACTION1 proteins', *The Plant Journal*, 101(3), pp. 619–636. doi:
326 10.1111/tpj.14566.

327 Duan, Q. *et al.* (2010) 'FERONIA receptor-like kinase regulates RHO GTPase signaling of
328 root hair development', *Proceedings of the National Academy of Sciences of the United*
329 *States of America*, 107(41), pp. 17821–17826. doi: 10.1073/pnas.1005366107.

330 Dünser, K. *et al.* (2019) 'Extracellular matrix sensing by <scp>FERONIA</scp> and Leucine-
331 Rich Repeat Extensins controls vacuolar expansion during cellular elongation in *Arabidopsis*
332 *thaliana*', *The EMBO Journal*, 38(7). doi: 10.15252/embj.2018100353.

333 Feng, W. *et al.* (2018) 'The FERONIA Receptor Kinase Maintains Cell-Wall Integrity during
334 Salt Stress through Ca 2+ Signaling', *Current Biology*, 28, pp. 666-675.e5. doi:
335 10.1016/j.cub.2018.01.023.

336 Feraru, E. *et al.* (2011) 'PIN polarity maintenance by the cell wall in Arabidopsis', *Current*
337 *Biology*, 21(4), pp. 338–343. doi: 10.1016/j.cub.2011.01.036.

338 Franck, C. M., Westermann, J. and Boisson-Dernier, A. (2018) 'Plant Malectin-Like Receptor
339 Kinases: From Cell Wall Integrity to Immunity and Beyond', *Annual Review of Plant Biology*,
340 69(1), pp. 301–328. doi: 10.1146/annurev-arplant-042817-040557.

341 Ge, Z. *et al.* (2017) 'Arabidopsis pollen tube integrity and sperm release are regulated by
342 RALF-mediated signaling', *Science*, 358(6370), pp. 1596–1600. doi:
343 10.1126/science.aao3642.

344 Göhre, V. *et al.* (2008) 'Plant Pattern-Recognition Receptor FLS2 Is Directed for Degradation
345 by the Bacterial Ubiquitin Ligase AvrPtoB', *Current Biology*, 18(23), pp. 1824–1832. doi:
346 10.1016/j.cub.2008.10.063.

347 Gómez-Gómez, L. and Boller, T. (2000) 'FLS2: An LRR receptor-like kinase involved in the
348 perception of the bacterial elicitor flagellin in Arabidopsis', *Molecular Cell*, 5(6), pp. 1003–
349 1011. doi: 10.1016/S1097-2765(00)80265-8.

350 Gonneau, M. *et al.* (2018) 'Receptor Kinase THESEUS1 Is a Rapid Alkalinization Factor 34
351 Receptor in Arabidopsis', *Current Biology*, 28(15), pp. 2452-2458.e4. doi:
352 10.1016/j.cub.2018.05.075.

353 Gronnier, J. *et al.* (2017) 'Structural basis for plant plasma membrane protein dynamics and
354 organization into functional nanodomains', *eLife*, 6, pp. 1–24. doi: 10.7554/eLife.26404.

355 Gronnier, J. *et al.* (2018) 'Divide and Rule: Plant Plasma Membrane Organization', *Trends in*
356 *Plant Science*, 23(10). doi: 10.1016/j.tplants.2018.07.007.

357 Gronnier, J. *et al.* (2019) 'Mechanisms governing subcompartmentalization of biological
358 membranes', *Current Opinion in Plant Biology*, 52. doi: 10.1016/j.pbi.2019.08.003.

359 Grossmann, G. *et al.* (2008) 'Plasma membrane microdomains regulate turnover of transport
360 proteins in yeast', *Journal of Cell Biology*, 183(6), pp. 1075–1088. doi:
361 10.1083/jcb.200806035.

362 Haruta, M. *et al.* (2014) 'A peptide hormone and its receptor protein kinase regulate plant cell
363 expansion', *Science*, 343(6169), pp. 408–411. doi: 10.1126/science.1244454.

364 Herger, A. *et al.* (2019) 'Leucine-Rich Repeat Extensin Proteins and Their Role in Cell Wall
365 Sensing', *Current Biology*. Cell Press, pp. R851–R858. doi: 10.1016/j.cub.2019.07.039.

366 Herger, A. *et al.* (2020) 'Overlapping functions and protein-protein interactions of LRR-
367 extensins in Arabidopsis', *PLOS Genetics*. Edited by G. K. Muday, 16(6), p. e1008847. doi:
368 10.1371/journal.pgen.1008847.

369 Hohmann, U., Lau, K. and Hothorn, M. (2017) 'The Structural Basis of Ligand Perception and
370 Signal Activation by Receptor Kinases', *Annu. Rev. Plant Biol*, 68, pp. 109–37. doi:
371 10.1146/annurev-arplant-042916.

372 Hutten, S. J. *et al.* (2017) 'Visualization of BRI1 and SERK3/BAK1 Nanoclusters in
373 Arabidopsis Roots', *Plos One*, 12(1), p. e0169905. doi: 10.1371/journal.pone.0169905.

374 Jacobson, K., Liu, P. and Lagerholm, B. C. (2019) 'The Lateral Organization and Mobility of
375 Plasma Membrane Components', *Cell*. Cell Press, pp. 806–819. doi:
376 10.1016/j.cell.2019.04.018.

377 Jaillais, Y. and Ott, T. (2020) 'The Nanoscale Organization of the Plasma Membrane and Its
378 Importance in Signaling: A Proteolipid Perspective', *Plant Physiology*, 182(4), pp. 1682–
379 1696. doi: 10.1104/pp.19.01349.

380 Jaqaman, K. *et al.* (2008) 'Robust single-particle tracking in live-cell time-lapse sequences',
381 *Nature Methods*, 5(8), pp. 695–702. doi: 10.1038/nmeth.1237.

382 Kadota, Y. *et al.* (2014) 'Direct Regulation of the NADPH Oxidase RBOHD by the PRR-
383 Associated Kinase BIK1 during Plant Immunity', *Molecular Cell*, 54, pp. 43–55. doi:
384 10.1016/j.molcel.2014.02.021.

385 Liang, P. *et al.* (2018) 'Symbiotic root infections in Medicago truncatula require remorin-
386 mediated receptor stabilization in membrane nanodomains', *Proceedings of the National*
387 *Academy of Sciences of the United States of America*, 115(20), pp. 5289–5294. doi:
388 10.1073/pnas.1721868115.

389 Lin, W. *et al.* (2018) 'FERONIA's sensing of cell wall pectin activates ROP GTPase signaling
390 in Arabidopsis', *bioRxiv*, 35(June), p. 269647. doi: 10.1101/269647.

391 Liu, C. *et al.* (2021) 'Pollen PCP-B peptides unlock a stigma peptide–receptor kinase gating
392 mechanism for pollination', *Science*, 372(6538), pp. 171–175. doi:
393 10.1126/SCIENCE.ABC6107.

394 Martinière, A. *et al.* (2012) 'Cell wall constrains lateral diffusion of plant plasma-membrane
395 proteins.', *Proceedings of the National Academy of Sciences of the United States of America*,
396 109(31), pp. 12805–10. doi: 10.1073/pnas.1202040109.

397 McKenna, J. F. *et al.* (2019) 'The cell wall regulates dynamics and size of plasma-membrane
398 nanodomains in Arabidopsis', *Proceedings of the National Academy of Sciences of the*
399 *United States of America*, 116(26), pp. 12857–12862. doi: 10.1073/pnas.1819077116.

400 Mecchia, M. A. *et al.* (2017) 'RALF4/19 peptides interact with LRX proteins to control pollen
401 tube growth in Arabidopsis', *Science*, 358(6370), pp. 1600–1603. doi:
402 10.1126/science.aao5467.

403 Moussu, S. *et al.* (2018) 'Crystal structures of two tandem malectin-like receptor kinases
404 involved in plant reproduction', *research papers Acta Cryst*, 74, pp. 671–680. doi:
405 10.1107/S205979831800774X.

406 Moussu, S. *et al.* (2020) 'Structural basis for recognition of RALF peptides by LRX proteins
407 during pollen tube growth', *Proceedings of the National Academy of Sciences of the United*
408 *States of America*, 117(13), pp. 7494–7503. doi: 10.1073/pnas.2000100117.

409 Perraki, A. *et al.* (2018) 'Phosphocode-dependent functional dichotomy of a common co-
410 receptor in plant signalling', *Nature*, 561(7722), pp. 248–252. doi: 10.1038/s41586-018-0471-
411 x.

412 Roux, M. *et al.* (2011) 'The Arabidopsis leucine-rich repeat receptor-like kinases
413 BAK1/SERK3 and BKK1/SERK4 are required for innate immunity to hemibiotrophic and
414 biotrophic pathogens', *Plant Cell*, 23(6), pp. 2440–2455. doi: 10.1105/tpc.111.084301.

415 Schindelin, J. *et al.* (2012) 'Fiji: an open-source platform for biological-image analysis',
416 *Nature Methods 2012 9:7*, 9(7), pp. 676–682. doi: 10.1038/nmeth.2019.

417 Schulze, B. *et al.* (2010) 'Rapid heteromerization and phosphorylation of ligand-activated
418 plant transmembrane receptors and their associated kinase BAK1', *Journal of Biological*
419 *Chemistry*, 285(13), pp. 9444–9451. doi: 10.1074/jbc.M109.096842.

420 Schwessinger, B. *et al.* (2011) 'Phosphorylation-Dependent Differential Regulation of Plant
421 Growth, Cell Death, and Innate Immunity by the Regulatory Receptor-Like Kinase BAK1',
422 *PLoS Genetics*. Edited by D. S. Guttman, 7(4), p. e1002046. doi:
423 10.1371/journal.pgen.1002046.

424 Stegmann, M. *et al.* (2017) 'The receptor kinase FER is a RALF-regulated scaffold controlling
425 plant immuneTraduire I'll send you everything by tomorrow night that you could send to all
426 authors by the end of this week. 102/5000 Je vous enverrai tout demain soir que vous
427 pourriez envoy', 4(January), pp. 287–289. doi: 10.1126/science.aal2541.

428 Sun, Y. *et al.* (2013) 'Structural basis for flg22-induced activation of the Arabidopsis FLS2-
429 BAK1 immune complex', *Science*, 342(6158), pp. 624–628. doi: 10.1126/science.1243825.

430 Tinevez, J. Y. *et al.* (2017) 'TrackMate: An open and extensible platform for single-particle
431 tracking', *Methods*, 115, pp. 80–90. doi: 10.1016/j.ymeth.2016.09.016.

432 Tran, T. M. *et al.* (2020) 'The bacterial quorum sensing signal DSF hijacks Arabidopsis
433 thaliana sterol biosynthesis to suppress plant innate immunity', *Life Science Alliance*, 3(10).
434 doi: 10.26508/LSA.202000720.

Wagner, T. *et al.* (2017) ‘Classification and Segmentation of Nanoparticle Diffusion Trajectories in Cellular Micro Environments’, *PLOS ONE*. Edited by B. Xu, 12(1), p. e0170165. doi: 10.1371/journal.pone.0170165.

Xiao, Y. *et al.* (2019) ‘Mechanisms of RALF peptide perception by a heterotypic receptor complex’, *Nature*, 572(7768), pp. 270–274. doi: 10.1038/s41586-019-1409-7.

Yu, X. *et al.* (2017) ‘From Chaos to Harmony: Responses and Signaling upon Microbial Pattern Recognition’, *Annual Review of Phytopathology*, 55(1), pp. 109–137. doi: 10.1146/annurev-phyto-080516-035649.

Zhao, C. *et al.* (2018) ‘Leucine-rich repeat extensin proteins regulate plant salt tolerance in Arabidopsis’, *Proceedings of the National Academy of Sciences of the United States of America*, 115(51), pp. 13123–13128. doi: 10.1073/pnas.1816991115.

Zipfel, C. *et al.* (2006) ‘Perception of the Bacterial PAMP EF-Tu by the Receptor EFR Restricts Agrobacterium-Mediated Transformation’, *Cell*, 125(4), pp. 749–760. doi: 10.1016/j.cell.2006.03.037.

451 **FIGURE LEGENDS**

452 **Fig. 1 ¦ FER regulates the nanoscale organization of FLS2-GFP and BAK1-mCherry**

453 **A and E**. FLS2-GFP and BAK1-mCherry nanodomain organization. Pictures are maximum
454 projection images of FLS2-GFP (**A**) and BAK1-mCherry (**E**) in Col-0 and *fer-4* cotyledon
455 epidermal cells.
456 **B and F**. Representative kymograph showing lateral organization of FLS2-GFP (**B**) and BAK1-
457 mCherry (**F**) overtime in Col-0 and *fer-4*.
458 **C and G**. Quantification of FLS2-GFP (**C**) and BAK1-mCherry (**G**) spatial clustering index. Red
459 crosses and red horizontal lines show mean and SEM, P values reports non-parametric Mann-
460 Whitney test. Similar results were obtained in three independent experiments.
461 **D and H**. Proposed graphical summary of our observations for FLS2-GFP (**D**) and BAK1-
462 mCherry (**H**) nanoscale dynamics.
463

464 **Fig. 2 ¦ LRX3, LRX4 and LRX5 regulate PTI and BAK1-mCherry organization.**

465 **A**. flg22-induced FLS2-BAK1 complex formation. Immunoprecipitation of FLS2 in Arabidopsis
466 Col-0 and *lr3/4/5* seedlings either untreated or treated with 100 nM flg22 for 10 min. Blot
467 stained with CBB is presented to show equal loading. Western blots were probed with α-FLS2,
468 α-BAK1, or α-FER antibodies. Similar results were obtained in at least three independent
469 experiments.
470 **B-C**. ROS production after elicitation with 100 nM elf18 (**B**), or 100 nM flg22 (**C**). Values are
471 means of total photon counts over 40 min. Red crosses and red horizontal lines denote mean
472 and SEM, n = 32. Conditions which do not share a letter are significantly different in Dunn's
473 multiple comparison test ($p < 0.0001$).
474 **D**. BAK1-mCherry nanodomain organization. Pictures are maximum projection images (20
475 TIRFM images obtained at 2.5 frames per second) of BAK1-mCherry in Col-0, *fer-4* and
476 *lrx3/4/5* cotyledon epidermal cells.
477 **E**. Representative kymograph showing lateral organization of BAK1-mCherry overtime in Col-
478 0, *fer-4* and *lrx3/4/5*.
479 **F**. Quantification of BAK1-mCherry spatial clustering index, red crosses and red horizontal
480 lines show mean and SEM. Conditions which do not share a letter are significantly different in
481 Dunn's multiple comparison test ($p < 0.001$). Similar results were obtained in three independent
482 experiments.
483 **G**. Proposed graphical summary of our observations for BAK1-mCherry nanoscale dynamics
484 in *lrx3/4/5*.
485

486

487 **Fig. 3 ¦ FER malectin A domain regulates cell morphogenesis not PTI**

488 **A**. Proposed graphical representation of RALF23 perception by FER-LLG1 complex.
489 **B**. Morphology of 4-week-old Arabidopsis plants, scale bar indicates 5 cm.
490 **C-D**. Confocal microscopy pictures of 5-day-old seedlings cotyledon (**C**) and root (**D**) stained
491 with propidium iodide. Similar results were obtained in at least three independent experiments.
492 **E**. flg22-induced FLS2-BAK1 complex formation. Immunoprecipitation of FLS2 in Arabidopsis
493 Col-0, *fer-4*, and *fer-4*/p35S::FER$^{\Delta MalA}$-YFP seedlings that were either untreated or treated with
494 100 nM flg22 for 10 min. Blot stained with Coomassie brilliant blue (CBB) is presented to show
495 equal loading. Western blots were probed with α-FLS2, α-BAK1, or α-FER antibodies. Similar
496 results were obtained in at least three independent experiments.
497 **F-G**. ROS production after elicitation with 100 nM flg22 (**F**), or 100 nM elf18 (**G**). Values are
498 means of total photon counts over 40 min, n = 8. Red crosses and red horizontal lines denote
499 mean and SEM, respectively. Conditions which do not share a letter are significantly different
500 in Dunn's multiple comparison test ($p < 0.0001$).
501 **H**. Fresh weight of 12-day-old seedlings grown in the absence (mock) or presence of 1 μM of
502 RALF23 peptide. Fresh weight is expressed as relative to the control mock condition. Similar
503 results were obtained in at least three independent experiments. Conditions which do not share
504 a letter are significantly different in Dunn's multiple comparison test ($p < 0.001$).
505

506 **Fig. 4 ¦ RALF23 perception regulates BAK1-mCherry organization.**

507 **A**. BAK1-mCherry nanodomain organization (pBAK1::BAK1-mCherry). Pictures are maximum
508 projection images of BAK1-mCherry in Col-0 and *fer-4* cotyledon epidermal cells with or without
509 1 μM RALF23 treatment (2 to 30 min).
510 **B**. Representative kymograph showing lateral organization of BAK1-mCherry overtime in Col-
511 0 and *fer-4* with or without 1 μM RALF23 treatment.
512 **C**. Quantification of BAK1-mCherry spatial clustering index, red crosses and red horizontal
513 lines show mean and SEM. Conditions which do not share a letter are significantly different in
514 Dunn's multiple comparison test ($p < 0.001$). Similar results were obtained in three independent
515 experiments.
516 **D**. Proposed graphical summary of our observations for BAK1-mCherry nanoscale dynamics
517 upon RALF23 treatment.
518

519 **Fig. S1 ¦ Analysis of FLS2-GFP single particle dynamics in *fer-4.***

520 **A**. Representative images of FLS2-GFP single-particles tracked in Col-0 and *fer-4* cotyledon
521 epidermal cells of 5-day-old seedlings.

522 **B**. Quantification of FLS2-GFP diffusion coefficient (D). Similar results were obtained in three
523 independent experiments.
524
525 **Fig. S2 ¦ Analysis of FLS2-GFP organization and dynamics in *fer-2.***

526 **A**. Representative images of FLS2-GFP single-particles tracked in Col-0 and *fer-2* cotyledon
527 epidermal cells of 5-day-old seedlings.
528 **B**. Quantification of FLS2-GFP diffusion coefficient (D). Similar results were obtained in three
529 independent experiments.
530 **C**. Pictures are maximum projection images of FLS2-GFP in Col-0 and *fer-2* cotyledon
531 epidermal cells.
532 **D**. Quantification of FLS2-GFP spatial clustering index in Col-0 and *fer-2*. Red crosses and red
533 horizontal lines show mean and SEM, P values reports non-parametric Mann-Whitney test.
534 Similar results were obtained in three independent experiments.
535
536 **Fig. S3 ¦ FLS2-GFP accumulation at the PM is altered in *fer* mutants.**

537 **A-D**. Representative confocal microscopy pictures of FLS2-GFP driven by its native promoter
538 in Col-0 and *fer-2* (**A**) and *fer-4* (**C**) cotyledon epidermal cells of 5-day-old seedlings. Scale bar
539 indicate 2 µm. Quantification of FLS2-GFP fluorescence intensity at the plasma membrane in
540 Col-0 and *fer-2* (**B**) and *fer-4* (**D**) cotyledon epidermal cells of 5-day-old seedlings. Two-way
541 student's t test. Similar results were obtained in at least three independent experiments.

542
543 **Fig. S4 ¦ Subcellular localization of BAK1-mCherry in *fer-4* and *lrx3/4/5.***

544 **A**. Representative confocal microscopy pictures of BAK1-mCherry driven by its native
545 promoter in Col-0, *fer-4* and *lrx3/4/5* cotyledon epidermal cells of 5-day-old seedlings. Scale
546 bar indicates 20 µm.
547 **B**. Quantification of BAK1-mCherry fluorescence intensity at the plasma membrane. Letters
548 indicate a Dunn's multiple comparison statistical test.
549
550 **Fig. S5 ¦ *LRX3, LRX4* and *LRX5* are dispensable for FER plasma membrane localization**
551 **and accumulation.**

552 **A**. Accumulation of endogenous FER detected by western blot. Total proteins were extracted
553 from 2-week-old seedlings. Blot stained with CBB is presented to show equal loading.
554 **B-C**. Representative confocal microscopy pictures of FER-GFP driven by its native promoter
555 in *fer-4* and *lrx3/4/5* cotyledon epidermal cells (**B**) and root hair (**C**) of 5-day-old seedlings.
556 Scale bar indicates 20 µm.

557

558 **Fig. S6 ¦ *LRX3, LRX4* and *LRX5* are dispensable for FER-GFP nanoscale organization.**

559 **A**. FER-GFP nanodomain organization. Pictures are maximum projection images (20 TIRFM
560 images obtained at 5 frames per second) of FER-GFP in *fer-4* and *lrx3/4/5* cotyledon epidermal
561 cells.
562 **B**. Representative kymograph showing lateral organization of FER-GFP overtime in *fer-4* and
563 *lrx3/4/5*.
564 **C**. Quantification of FER-GFP spatial clustering index. Red crosses and red horizontal lines
565 show mean and SEM. Conditions which do not share a letter are significantly different in
566 Dunn's multiple comparison test ($p < 0.001$). Similar results were obtained in three independent
567 experiments.
568 **D**. Proposed graphical summary of our observations for FER-GFP nanoscale dynamics.
569

570 **Fig. S7 ¦ LRX3, LRX4 and LRX5 contribute to RALF23 responsiveness.**

571 **A**. ROS production in Col-0 and *lr3/4/5* leaf discs treated with 100 nM elf18 and with or without
572 1 μM RALF23 co-treatment in 2 mM MES–KOH pH 5.8. Values are means of total photon
573 counts over 40 min. Red crosses and red horizontal lines show mean and SEM, n = 12.
574 Conditions which do not share a letter are significantly different in Dunn's multiple comparison
575 test ($p < 0.0001$).
576 **B**. Fresh weight of 12-day-old seedlings grown in the absence (mock) or presence of 1 μM of
577 RALF23 peptide. Fresh weight is expressed as relative to the control mock condition. Similar
578 results were obtained in at least three independent experiments. Conditions which do not share
579 a letter are significantly different in Dunn's multiple comparison test ($p < 0.001$).
580 **C**. Proposed graphical representation of LRX3/4/5 as potential receptors for RALF23.
581

582 **Fig. S8 ¦ RALF23 does not modulate constitutive association between FER and LRX4.**

583 Immunoprecipitation of LRX4$^{\Delta E}$-FLAG in Arabidopsis seedlings untreated or treated with 1 μM
584 RALF23 for 10 min. Western blots were probed with α-FLAG or α-FER antibodies. Blot stained
585 with CBB is presented to show equal loading. Similar results were obtained in at least three
586 independent experiments.

587

588

589 **Fig. S9 ¦ Overexpression of LRX4$^{\Delta E}$ does not affect PTI.**

590 **A**. flg22-induced FLS2-BAK1 complex formation. Immunoprecipitation of FLS2 in Arabidopsis
591 seedlings either untreated or treated with 100 nM flg22 for 10 min. Blot stained with CBB is
592 presented to show equal loading. Western blots were probed with α-FLS2 and α-BAK1
593 antibodies.
594 **B-C**. ROS production after elicitation with 100 nM flg22 (B), or 100 nM elf18 (C). Values are
595 means of total photon counts over 40 min. Red crosses and red horizontal lines denote mean
596 and SEM. Conditions which do not share a letter are significantly different in Dunn's multiple
597 comparison test ($p < 0.0001$). Similar results were obtained in at least three independent
598 experiments.
599 **D.** Root length of 6-day-old seedlings incubated for 3 days in liquid MS medium with or without
600 indicated concentration of flg22. Red crosses and red horizontal lines denote mean and SEM.
601 Conditions which do not share a letter are significantly different in Brown-Forsythe and Welch
602 ANOVA multiple comparison test ($p < 0.001$), n= 9-12 seedlings per condition. Similar results
603 were obtained in at least three independent experiments.
604 **E**. Fresh weight of 12-day-old seedlings grown in the absence (mock) or presence of 1 μM of
605 RALF23 peptide. Fresh weight is expressed as relative to the control mock condition. Similar
606 results were obtained in at least three independent experiments. Conditions which do not share
607 a letter are significantly different in Dunn's multiple comparison test ($p < 0.001$).
608

609 **Fig. S10 ¦ FER kinase activity is dispensable to support PTI signaling.**

610 **A**. flg22-induced FLS2-BAK1 complex formation. Immunoprecipitation of FLS2 in Arabidopsis
611 Col-0, *fer-4*, and *fer-4*/pFER::FER^{KD}-GFP seedlings that were either untreated or treated with
612 100 nM flg22 for 10 min. Blot stained with Coomassie brilliant blue (CBB) is presented to show
613 equal loading. Western blots were probed with α-FLS2, α-BAK1, α-BAK1-pS612 or α-FER
614 antibodies. Similar results were obtained in at least three independent experiments.
615 **B-C**. ROS production after elicitation with 100 nM flg22 (**A**), or 100 nM elf18 (**B**). Values are
616 means of total photon counts over 40 min, $n = 16$. Red crosses and red horizontal lines denote
617 mean and SEM, respectively. Conditions which do not share a letter are significantly different
618 in Dunn's multiple comparison test ($p < 0.0001$).
619

620 **Fig. S11 ¦ Inhibition of PTI signaling by RALF23 requires FER kinase activity.**

621 **A.** Accumulation of endogenous FER and FER^{K565R}-GFP detected by western blot. Total
622 proteins were extracted from 2-week-old seedlings. Blot stained with CBB is presented to show
623 loading.
624

625 **B.** flg22-induced FLS2-BAK1 complex formation. Immunoprecipitation of FLS2 in Arabidopsis
626 *fer-2*, and *fer-2*/pFER::FER^{K565R}-GFP seedlings that were either untreated or treated with 100
627 nM of flg22 and 1 μM RALF23 for 10 min. Western blots were probed with α-FLS2, α-BAK1
628 antibodies.

629 **C**. ROS production after elicitation with 100 nM elf18, with and without 1 μM RALF23 co-
630 treatment. Values are means of total photon counts over 40 min, n = 10. Red crosses and red
631 horizontal lines denote mean and SEM, respectively. Conditions which do not share a letter
632 are significantly different in Dunn's multiple comparison test ($p < 0.05$). Similar results were
633 obtained in at least three independent experiments.

634 **Fig. S12 ¦ Analysis of FLS2-GFP single particle dynamics upon RALF23 treatment.**

635 **A**. Representative super-resolved images of FLS2-GFP single-particles tracked in Col-0 and
636 *fer-2* cotyledon epidermal cells of 5-day-old seedlings with or without 1 μM RALF23 treatment.

637 **B.** and quantification of FLS2-GFP diffusion coefficient (D) in Col-0 and *fer-2* with or without 1
638 μM RALF23 treatment. Data represent analysis of *ca* 1800 to 2900 single particles observed
639 across 14 to 18 cells. Individual data point represents the mean diffusion coefficient for each
640 cell. Red crosses and red horizontal lines show mean and SEM. Conditions which do not share
641 a letter are significantly different in Dunn's multiple comparison test ($p < 0.0001$). Similar results
642 were obtained in at least three independent experiments.

643 **Fig. S13 ¦ Analysis of FLS2-GFP organization upon RALF23 treatment.**

644 **A.** Pictures are maximum projection images (20 TIRFM images obtained at 20 frames per
645 second) of FLS2-GFP in Col-0 and *fer-2* cotyledon epidermal cells with or without 1 μM
646 RALF23 treatment.
647 **B.** Representative kymograph showing lateral organization of FLS2-GFP overtime in Col-0 and
648 *fer-2* cotyledon epidermal cells with or without 1 μM RALF23 treatment.
649 **C.** Quantification of FLS2-GFP spatial clustering index. Red crosses and red horizontal lines
650 show mean and SEM. Conditions which do not share a letter are significantly different in
651 Dunn's multiple comparison test ($p < 0.0001$). Similar results were obtained in at least three
652 independent experiments.
653

654 **Fig. S14 ¦ Time-resolved analysis of the spatial clustering index.**

655 Data points correspond to the average of the spatial clustering index measured over 5 min
656 windows for FLS2-GFP (**A**) and BAK1-mCherry (**B**) with or without 1 μM RALF23 treatment.
657 The first data point (5 min), corresponds to the value obtained between 2- and 3-min post
658 treatment. Acquisition approximately started 2 min after treatments, the time required for
659 sample mounting.

660 **Fig. S15 ¦ Linear regression analysis of the relationship between the spatial clustering**
661 **index and fluorescence intensity.**

662 Spatial clustering index is calculated as the ratio of the mean of the 5 % highest values to the
663 mean of 5 % lowest values of fluorescence intensity obtain on a plot line. Here, spatial
664 clustering index values were plotted against the mean fluorescence intensity of the
665 corresponding plot line for FLS2-GFP (**A**) and BAK1-mCherry (**B-C**). Linear regression
666 analyses show poor to no correlation between the spatial clustering index and fluorescence
667 intensity (R^2 ranking from 0.14 and 0.015).

668 **Movie S1 ¦ TIRFM imaging of FLS2-GFP in Col-0 and *fer-4*.**

669 Representative stream images acquisition of FLS2-GFP particles observed at the surface of
670 5-day-old cotyledon epidermal cells by TIRF microscopy at 5 frame per second.

671 **Movie S2 ¦ TIRFM imaging of BAK1-mCherry in Col-0 and *fer-4* with or without RALF23**
672 **treatment.**

673 Representative stream images acquisition of BAK1-mCherry observed at the surface of 5-day-
674 old cotyledon epidermal cells by TIRF microscopy at 2.5 frame per second, in Col-0 (A and B)
675 and *fer-4* (C and D) with (B and D) or without (A and C) 1 μM RALF23 treatment. Scale bar
676 indicates 2 μm.

677 **Movie S3 ¦ TIRFM imaging of BAK1-mCherry in Col-0 and *lrx3/4/5.***

678 Representative stream images acquisition of BAK1-mCherry observed at the surface of 5-day-
679 old cotyledon epidermal cells by TIRF microscopy at 2.5 frame per second, in Col-0 (A) and
680 *lrx3/4/5* (B). Scale bar indicates 2 μm.

681 **Movie S4 ¦ TIRFM imaging of FER-GFP in *fer-4* and *fer-4*;*lrx3/4/5.***

682 Representative stream images acquisition of FER-GFP observed at the surface of 5-day-old
683 cotyledon epidermal cells by TIRF microscopy at 5 frame per second, in *fer-4* (A) and *fer-*
684 *4;lrx3/4/5* (B). Scale bar indicates 2 μm.

685 **Movie S5 ¦ TIRFM imaging of FLS2-GFP in Col-0 with or without RALF23 treatment.**

686 Representative stream images acquisition of FLS2-GFP particles observed at the surface of
687 5-day-old cotyledon epidermal cells by TIRF microscopy at 5 frame per second. Scale bar
688 indicates 2 μm.

689 **Movie S6 ¦ TIRFM imaging of FLS2-GFP in *fer-4* with or without RALF23 treatment.**

690 Representative stream images acquisition of FLS2-GFP particles observed at the surface of
691 5-day-old cotyledon epidermal cells by TIRF microscopy at 5 frame per second. Scale bar
692 indicate 2 μm.

693 **Movie S7 ¦ TIRFM imaging of FLS2-GFP in Col-0 and *fer-2* with or without RALF23**
694 **treatment.**

695 Representative stream images acquisition of FLS2-GFP particles observed at the surface of
696 5-day-old cotyledon epidermal cells by TIRF microscopy at 20 frame per second. Scale bar
697 indicates 2 μm

698

699 **MATERIALS AND METHODS**

700 **Plant materials and growth**

701 *Arabidopsis thaliana* ecotype Columbia (Col-0) was used as WT control. The *fer-4, fer-*
702 *4/*pFER::FER-GFP (Duan *et al.*, 2010), *fer-4/*pFER::FER^{KD}-GFP (Chakravorty, Yu and
703 Assmann, 2018), *fer-4/*p35S::FER$^{\Delta MalA}$-GFP (Lin *et al.*, 2018), Col- 0/pFLS2::FLS2-GFP
704 (Göhre *et al.*, 2008), *fer-2*/pFLS2::FLS2-GFP (Stegmann *et al.*, 2017), *lrx3/4/5*, p35S::LRX4$^{\Delta E}$-
705 Citrine and p35S::LRX4$^{\Delta E}$-FLAG (Dünser *et al.*, 2019) lines were previously published. Col-
706 0/pFLS2::FLS2-GFP (Göhre *et al.*, 2008) was crossed with *fer-4* to obtain *fer-4/*pFLS2::FLS2-
707 GFP*.* Col-0/pBAK1::BAK1-mCherry (Bücherl *et al.*, 2013) was crossed with *fer-4* and *lrx3/4/*5
708 to obtain *fer*-4/pBAK1::BAK1-mCherry and *lrx3/4/5/*pBAK1::BAK1-mCherry. *fer-4/*pFER::FER-
709 GFP was crossed with *lrx3/4/5* to obtain *fer-4/lrx3/4/5;*pFER::FER-GFP. For ROS burst assays,
710 plants were grown in individual pots at 20-21 °C with a 10-h photoperiod in environmentally
711 controlled growth rooms. For seedling-based assays, seeds were surface-sterilized using
712 chlorine gas for 5 h and grown at 22 °C and a 16-h photoperiod on Murashige and Skoog (MS)
713 medium supplemented with vitamins, 1 % sucrose and 0.8 % agar.

714 **Synthetic peptides and chemicals**

715 The flg22, elf18, and RALF23 peptides were synthesized by EZBiolab (United States) with a
716 purity of >95 %. All peptides were dissolved in sterile purified water.

717 **ROS burst measurement**

718 ROS burst measurements were performed as previously documented (Kadota *et al.*, 2014). At
719 least eight leaf discs (4 mm in diameter) per individual genotype were collected in 96-well
720 plates containing sterile water and incubated overnight. The next day, the water was replaced
721 by a solution containing 17 µg/mL luminol (Sigma Aldrich), 20 µg/mL horseradish peroxidase
722 (HRP, Sigma Aldrich) and the peptides in the appropriate concentration. Luminescence was

723 measured for the indicated time period using a charge-coupled device camera (Photek Ltd.,
724 East Sussex UK). The effect of RALF23 on elf18-triggered ROS production was performed as
725 previously described (Stegmann *et al.*, 2017). Eight to ten leaf discs per treatment and/or
726 genotype were collected in 96-well plates containing water and incubated overnight. The
727 following day, the water was replaced by 75 µL of 2 mM MES-KOH pH 5.8 to mimic the
728 apoplastic pH. Leaf discs were incubated further for 4-5 h before adding 75 µL of a solution
729 containing 40 µg/mL HRP, 1 µM L-O12 (Wako Chemicals, Germany) and 2X elicitor RALF
730 peptide solution (final concentration 20 µg/mL HRP, 0.5 µM L-O12, 1x elicitors). ROS
731 production is displayed as the integration of total photon counts.

732 **Root growth inhibition assay**

733 Three-day-old Col-0, *fer-4*, *lrx3/4/5* and 35S::LRR4-Cit seedlings (n = 9-12) were transferred
734 for additional 3 days to 3 mL liquid ½ MS medium containing different concentrations (100 nM,
735 300 nM or 1 µM) of flg22 or the appropriate amount of solvent. The seedlings were then placed
736 on solid MS plates before scanning. Root length was measured using ImageJ.

737 **Live cell imaging**

738 For confocal microscopy and TIRF microscopy experiments, surface-sterilized seeds were
739 individually placed in line on square Petri dishes containing 1/2 MS 1 % sucrose, 0.8 %
740 phytoagar, stratified 2 d in the dark at 4 °C, then placed in a growth chamber at 22 °C and a
741 16-h photoperiod for 5 d. Seedlings were mounted between a glass slide and a coverslip in
742 liquid 1/2 MS, 1 % sucrose medium. To test the effect of RALF23 on FLS2-GFP dynamics and
743 nanodomain organization, seedlings were pre-incubated in 2 mM MES-KOH pH 5.8 for 3 to 4h
744 prior treatment. Seedlings were image 2-30 min after treatment.

745 **Confocal laser scanning microscopy (CLSM)**

746 Confocal microscopy was performed using a Leica SP5 CLSM system (Leica, Wetzlar,
747 Germany) equipped with Argon, DPSS, He-Ne lasers, hybrid detectors and using a 63X 1.2
748 NA oil immersion objective. GFP was excited using 488 nm argon laser and emission
749 wavelengths were collected between 495 and 550 nm. mCherry was excited using 561 nm
750 He/Ne laser and emission wavelengths were collected between 570 and 640 nm. Propidium
751 iodide was imaged using 488 nm and 500-550 nm excitation and emission wavelengths,
752 respectively. In order to obtain quantitative data, experiments were performed using strictly
753 identical confocal acquisition parameters (*e.g.* laser power, gain, zoom factor, resolution, and
754 emission wavelengths reception), with detector settings optimized for low background and no
755 pixel saturation. Pseudo-color images were obtained using look-up-table (LUT) of Fiji software
756 (Schindelin *et al.*, 2012).

757 **Total Internal Reflection Fluorescence (TIRF) microscopy**

758 TIRF microscopy was performed using an inverted Leica GSD equipped with a 160x objective
759 (NA = 1.43, oil immersion), and an Andor iXon Ultra 897 EMCCD camera. Images were
760 acquired by illuminating samples with a 488 nm solid state diode laser set at 15 mW, using a
761 cube filter with an excitation filter 488/10 and an emission filter 535/50 for FLS2-GFP and FER-
762 GFP. optimum critical angle was determined as giving the best signal-to-noise. Images time
763 series were recorded at 20 frames per second (50 ms exposure time) for Figure S11 and Figure
764 S3; 5 frames per second for Figure 1 and Figure S6. To observe BAK1-mCherry we could only
765 use a 532 nm solid state diode laser (*c.a* 40% of maximum excitation for mCherry), using a
766 cube filter with an excitation filter 532/10 and an emission filter 600/100. To obtain a sufficient
767 signal to noise ratio images time series were recorded at 2.5 frames per second (Figure 1, 2
768 and 5). Due to apparent high mobility of BAK1 and relatively slow acquisition rate we couldn't
769 asses with confidence the identity of fluorescent particles from one time frame to another and
770 therefore did not perform particle tracking analysis of BAK1-mCherry.

771 **Single particle tracking analysis**

772 To analyse single particle tracking experiments, we used the plugin TrackMate 2.7.4 (Tinevez
773 *et al.*, 2017) in Fiji (Schindelin *et al.*, 2012). Single particles were segmented frame-by-frame
774 by applying a LoG (Laplacian of Gaussian) filter and estimated particle size of 0.4 µm.
775 Individual single particle were localized with sub-pixel resolution using a built-in quadratic fitting
776 scheme. Then, single particle trajectories were reconstructed using a simple linear assignment
777 problem (Jaqaman *et al.*, 2008) with a maximal linking distance of 0.4 µm and without gap-
778 closing. Only tracks with at least ten successive points (tracked for 500 ms) were selected for
779 further analysis. Diffusion coefficients of individual particles were determined using
780 TraJClassifier (Wagner *et al.*, 2017). For each particle, the slope of the first four time points of
781 their mean square displacement (MSD) plot was used to calculate their diffusion coefficient
782 according to the following equation: $MSD= (x-x_0)^2+(y-y_0)^2$ and $D=MSD/4t$, where x0 and y0 are
783 the initial coordinates, and x and y are the coordinates at any given time, and *t* is the time
784 frame.

785 **Quantification of spatial clustering index**

786 Genotype and/or treatment dependent variation in fluorescence intensity of FLS2-GFP and
787 fluorescence pattern of FLS2-GFP and BAK1-mCherry compromised the use of a unique set
788 of parameters to compute nanodomain size and density across the different experiments. To
789 uniformly quantify differences in membrane organization of both FLS2 and BAK1 across all
790 experiments we used the spatial clustering index which was shown to be largely insensitive to
791 variation in fluorescence intensity (Gronnier *et al.*, 2017). Quantifications were performed as
792 previously described (Gronnier *et al.*, 2017). Briefly, fluorescence intensity was plotted along
793 an 8 µm long line on maximum projection TIRFM images, three plots were randomly recorded

794 per cell and, at least 8 cells per condition per experiment were analysed. For each line plot,
795 the spatial clustering index was calculated by dividing the mean of the 5 % highest values by
796 the mean of 5 % lowest values. Because the absence of correlation between fluorescence
797 intensity and spatial clustering index was assessed on confocal microscopy images and for a
798 single protein (Gronnier *et al.*, 2017), we decided to test if this was also the case in our
799 experimental conditions. Indeed, we consistently observed poor to no correlation between
800 variation in fluorescence intensity and values of spatial clustering index (Sup Fig. 15).

801 **Co-immunoprecipitation experiments**

802 Twenty to thirty seedlings per plate were grown in wells of a 6-well plate for 2 weeks,
803 transferred to 2 mM MES-KOH, pH 5.8 and incubated overnight. The next day, flg22, (final
804 concentration 100 nM) and/or RALF23 (final concentration 1 µM) were added and incubated
805 for 10 min. Seedlings were then frozen in liquid N2 and subjected to protein extraction. To
806 analyse FLS2-BAK1 receptor complex formation, proteins were isolated in 50 mM Tris-HCl pH
807 7.5, 150 mM NaCl, 10 % glycerol, 5 mM dithiothreitol, 1 % protease inhibitor cocktail (Sigma
808 Aldrich), 2 mM Na2MoO4, 2.5 mM NaF, 1.5 mM activated Na3VO4, 1 mM
809 phenylmethanesulfonyl fluoride and 0.5 % IGEPAL. For immunoprecipitations, α- rabbit
810 Trueblot agarose beads (eBioscience) coupled with α-FLS2 antibodies (Chinchilla *et al.,* 2007)
811 or GFP-Trap agarose beads (ChromoTek) were used and incubated with the crude extract for
812 3-4 h at 4 °C. Subsequently, beads were washed 3 times with wash buffer (50 mM Tris-HCl
813 pH 7.5, 150 mM NaCl, 1 mM phenylmethanesulfonyl fluoride, 0,1 % IGEPAL) before adding
814 Laemmli sample buffer and incubating for 10 min at 95 °C. Analysis was carried out by SDS-
815 PAGE and immunoblotting. To test the association between Flag-LRX4 and FER, total protein
816 from 60-90 seedlings per treatment per genotype was extracted as previously described. For
817 immunoprecipitations, M2 anti-Flag affinity gel (Sigma A2220-5ML) was used and incubated
818 with the crude extract for 2-3 h at 4 °C. Subsequently, beads were washed 3 times with wash
819 buffer (50 mM Tris-HCl pH 7.5, 150 mM NaCl, 1 mM phenylmethanesulfonyl fluoride, 0,1 %
820 IGEPAL) before adding Laemmli sample buffer and incubating for 10 min at 95 °C. Analysis
821 was carried out by SDS-PAGE and immunoblotting.

822 **Immunoblotting**

823 Protein samples were separated in 10 % bisacrylamide gels at 150 V for approximately 2 h
824 and transferred into activated PVDF membranes at 100 V for 90 min. Immunoblotting was
825 performed with antibodies diluted in blocking solution (5 % fat-free milk in TBS with 0.1 % (v/v)
826 Tween-20). Antibodies used in this study: α-BAK1 (1:5 000; (Roux *et al.*, 2011); α-FLS2
827 (1:1000; (Chinchilla et al., 2007); α-FER (1:2000; (Xiao *et al.*, 2019), α-BAK1 pS612 (1:3000;
828 (Perraki *et al.*, 2018)), α-FLAG-HRP (Sigma Aldrich, A8592, dilution 1:4000); α -GFP (sc-9996,
829 Santa Cruz, used at 1:5000). Blots were developed with Pierce ECL/ ECL Femto Western

830 Blotting Substrate (Thermo Scientific). The following secondary antibodies were used: anti-
831 rabbit IgG-HRP Trueblot (Rockland, 18-8816-31, dilution 1:10000) for detection of FLS2-BAK1
832 co-immunoprecipitation or anti-rabbit IgG (whole molecule)–HRP (A0545, Sigma, dilution
833 1:10000) for all other western blots.

834 **Statistical analysis**

835 Statistical analyses were carried out using Prism 6.0 software (GraphPad). As mentioned in
836 the figure legend, statistical significances were assessed using non-parametric Kruskal-Wallis
837 bilateral tests combined with post-hoc Dunn's multiple pairwise comparisons, or using a two-
838 way non-parametric student's t test Mann-Whitney test.

839 **Accession numbers**

840 FER (AT3G51550), LRX3 (AT4G13340), LRX4 (AT3G24480), LRX5 (AT4G18670), RALF23
841 (AT3G16570), FLS2 (AT5G46330), BAK1 (AT4G33430).

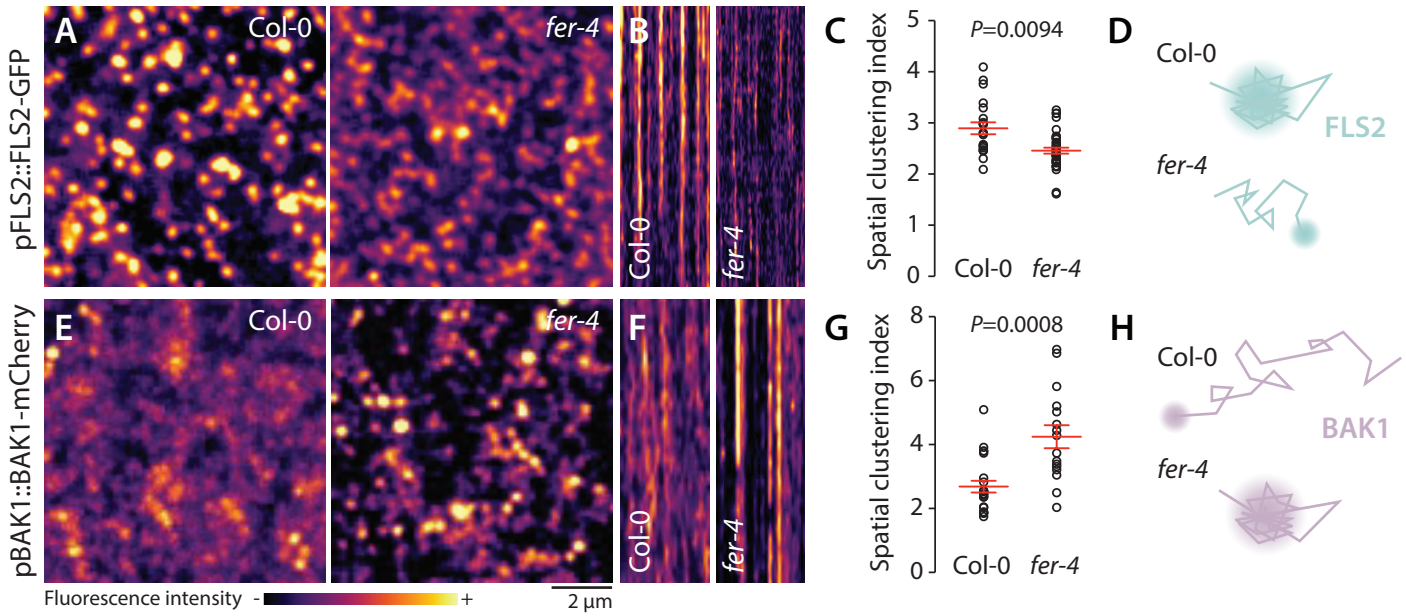

Fig. 1 ¦ FER regulates the nanoscale organization of FLS2-GFP and BAK1-mCherry

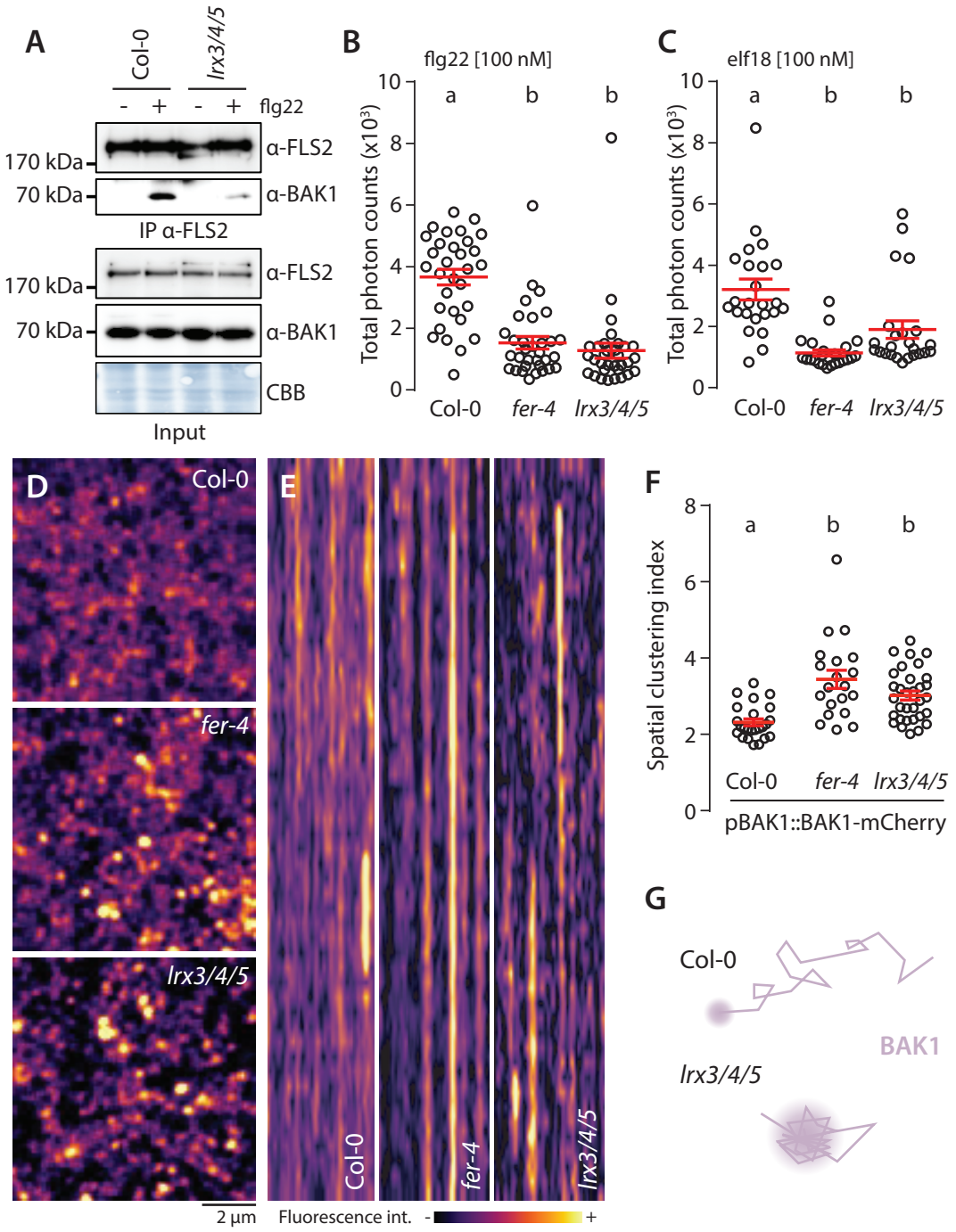

Fig. 2 ¦ LRX3, LRX4 and LRX5 regulate PTI and BAK1-mCherry organization.

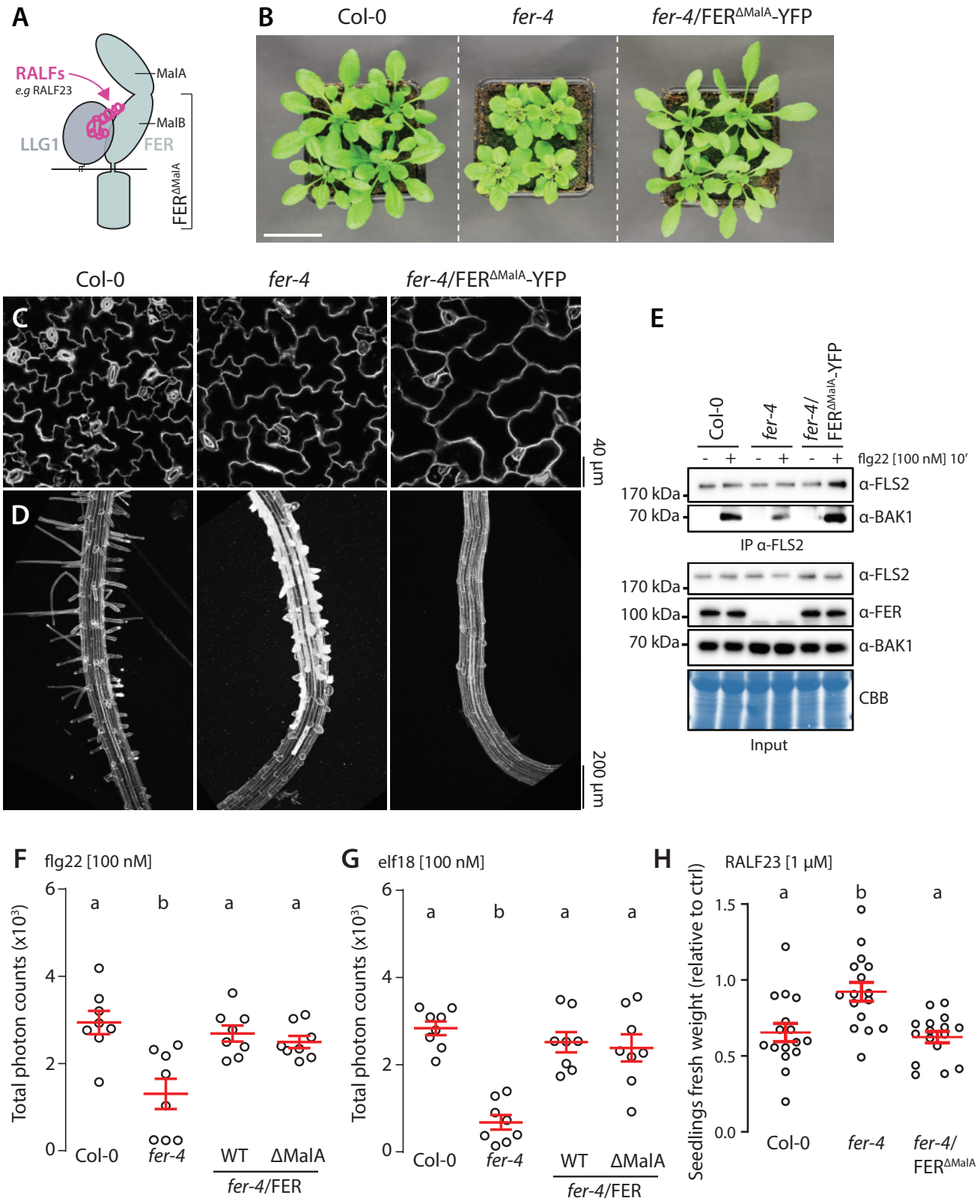

Fig. 3 ¦ FER malectin A domain regulates cell morphogenesis not PTI

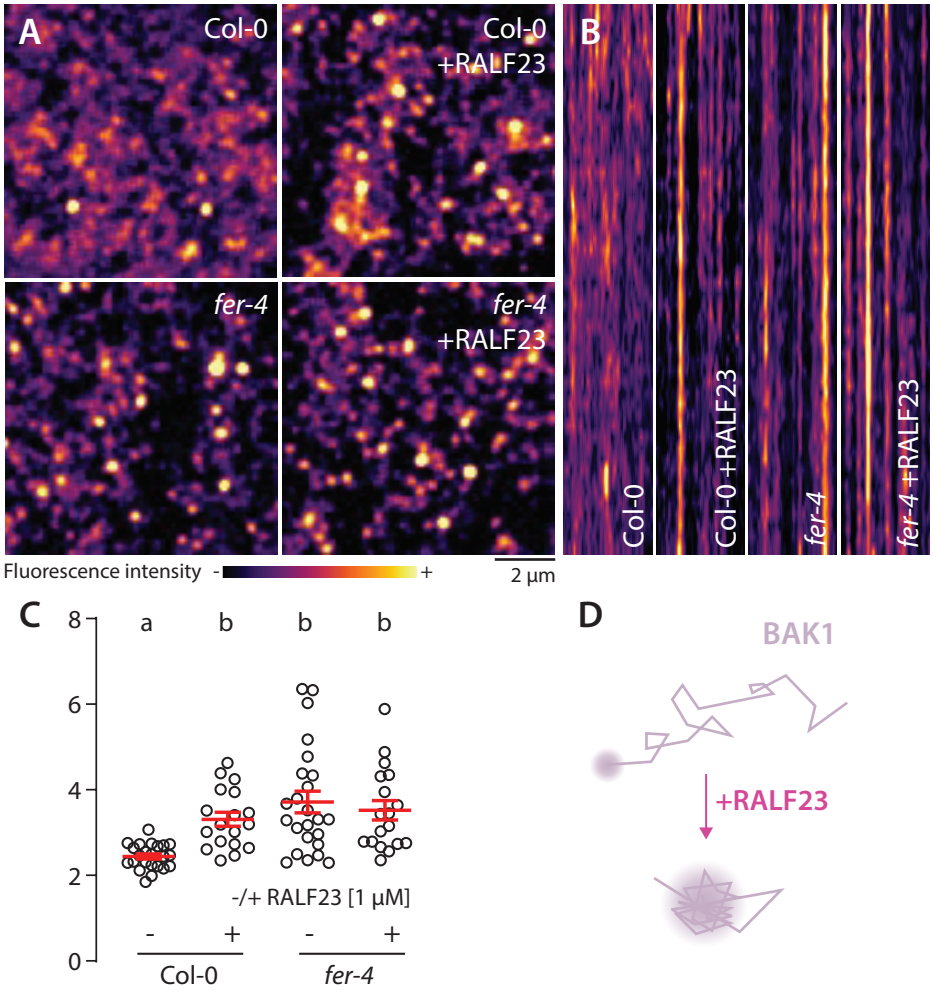

Fig. 4 ¦ RALF23 perception regulates BAK1-mCherry organization.

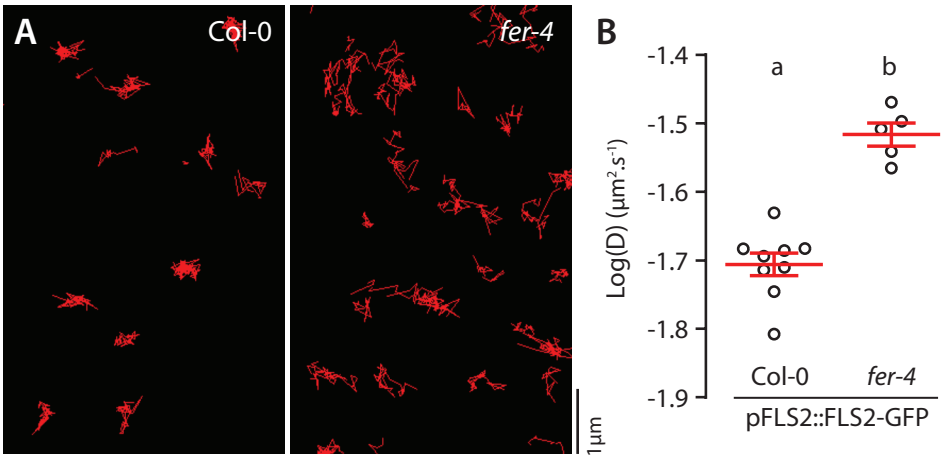

Fig. S1 ¦ Analysis of FLS2-GFP single particle dynamics in *fer-4*.

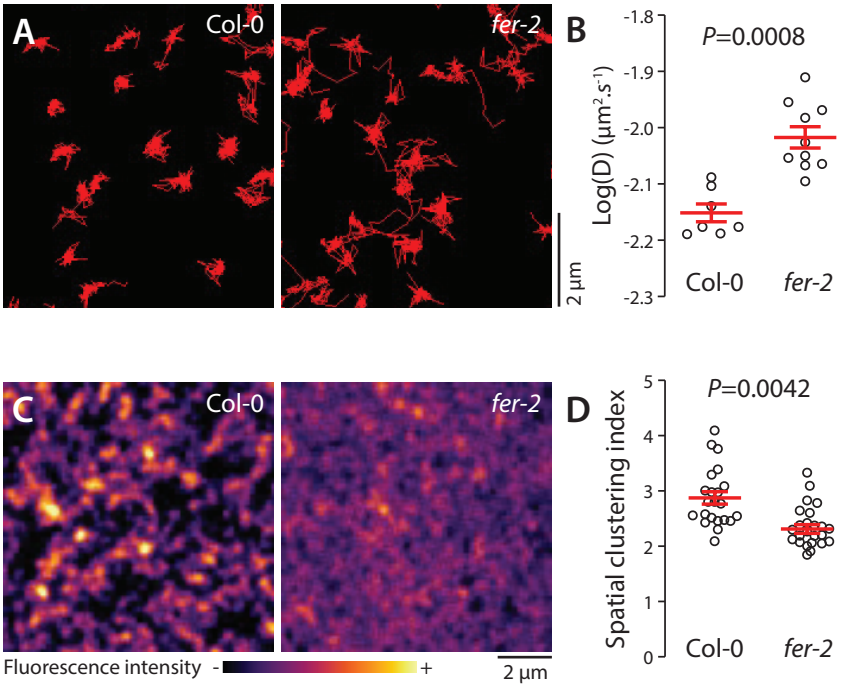

Fig. S2 ¦ Analysis of FLS2-GFP organization and dynamics in *fer-2*.

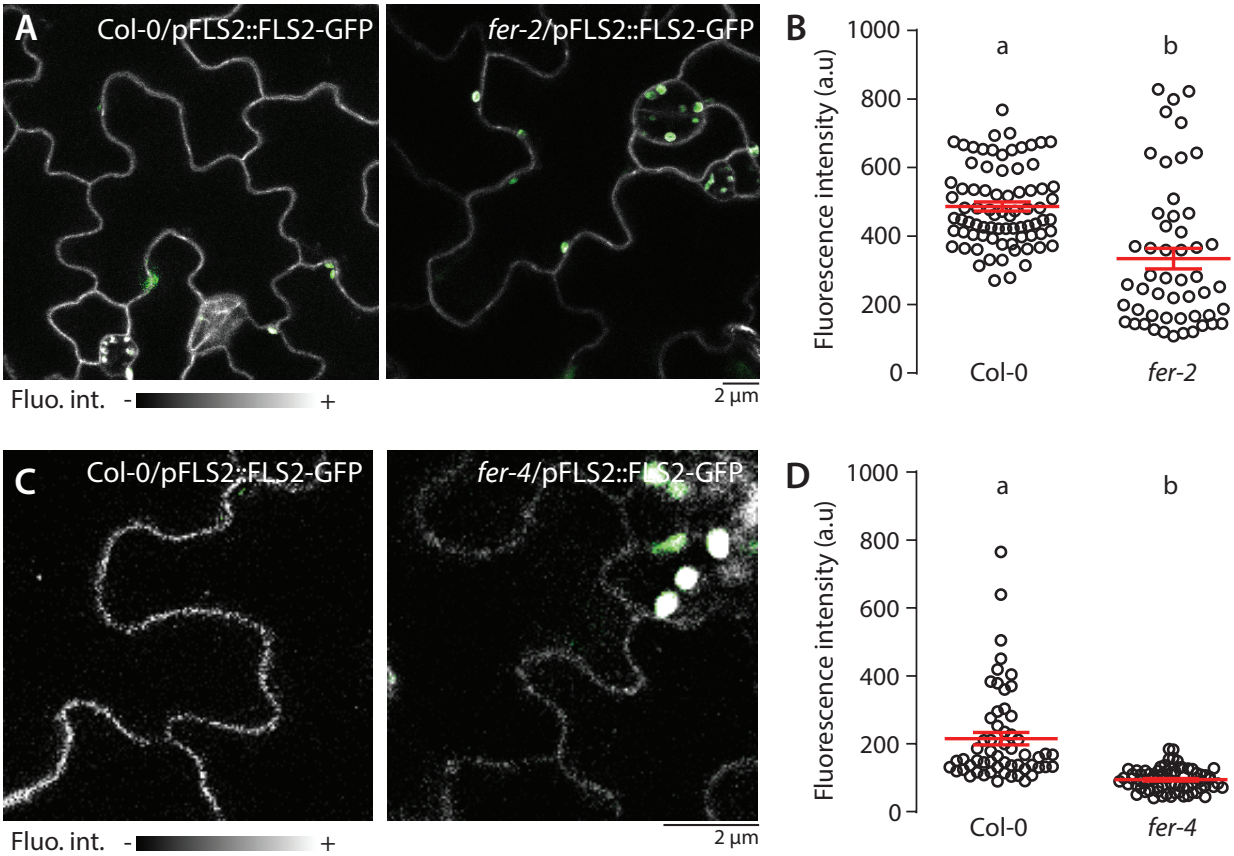

Fig. S3 ¦ FLS2-GFP accumulation at the PM is altered in *fer* mutants.

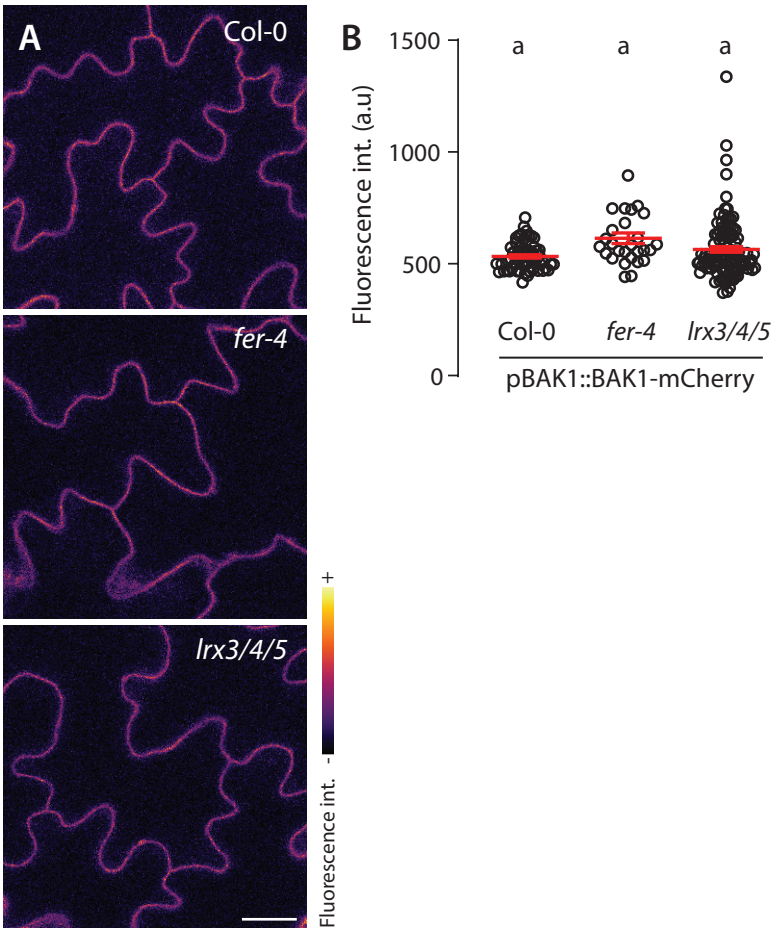

Fig. S4 ¦ Subcellular localization of BAK1-mCherry in *fer-4* and *lrx3/4/5*.

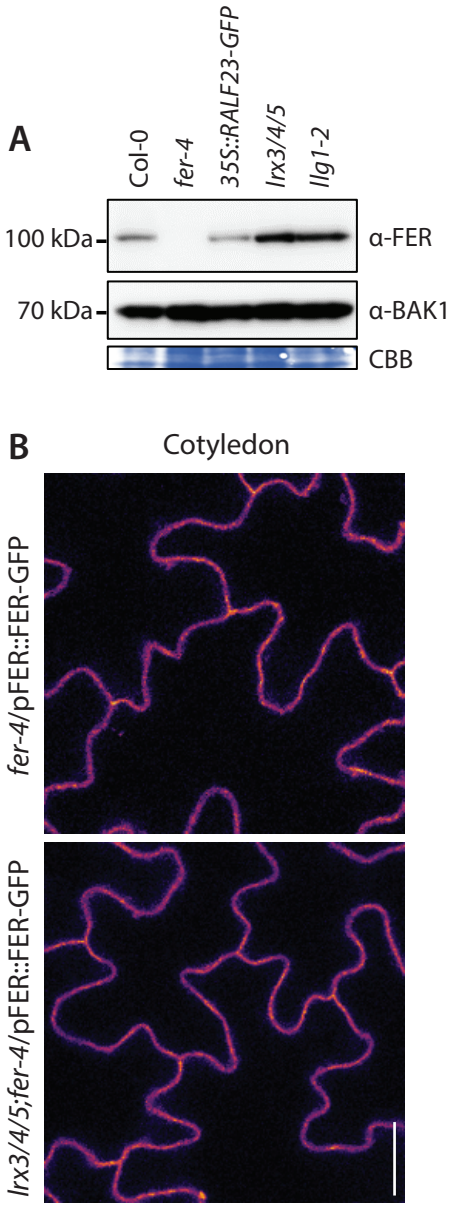

Fig. S5 ¦ *LRX3, LRX4 and LRX5* are dispensable for FER plasma membrane localization and accumulation.

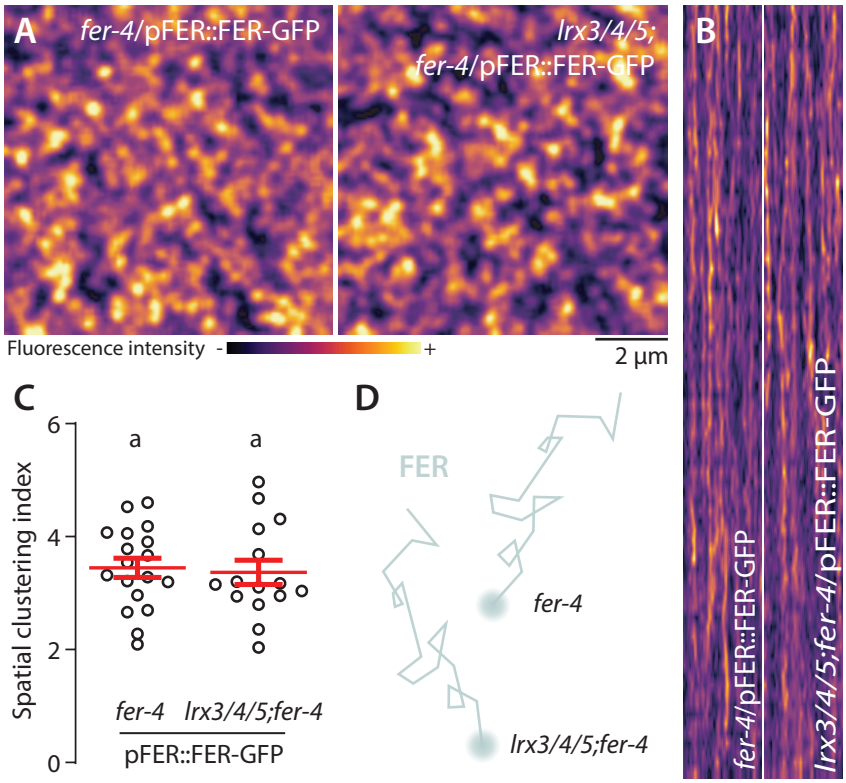

Fig. S6 ¦ LRX3, LRX4 and LRX5 are dispensable for FER-GFP nanoscale organization.

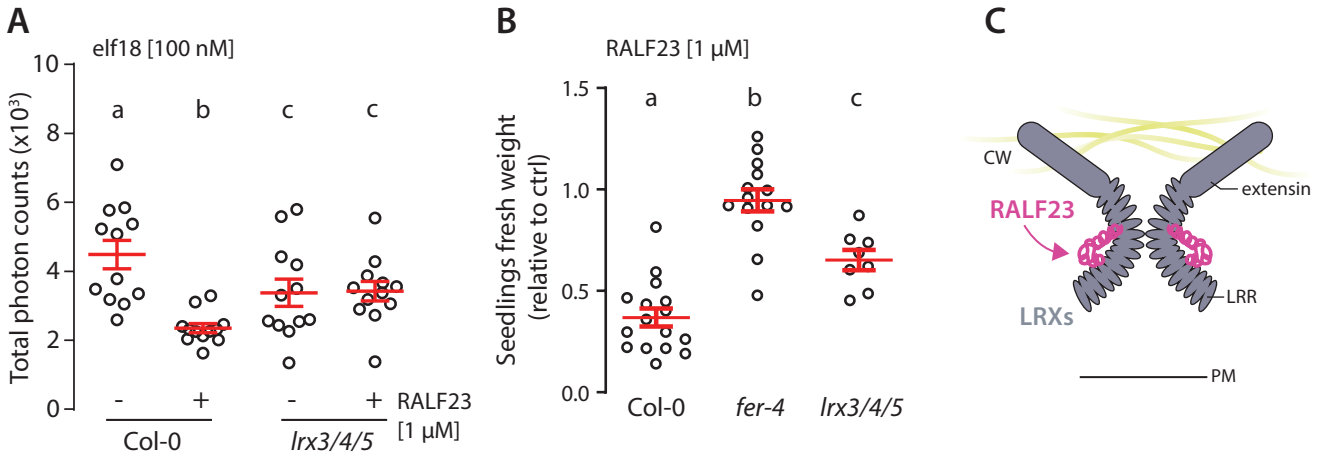

Fig. S7 ¦ LRX3, LRX4 and LRX5 contribute to RALF23 responsiveness.

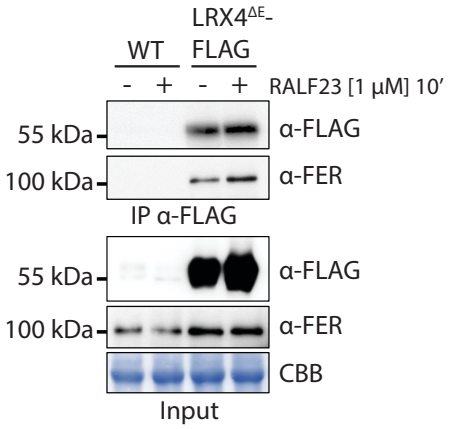

Fig. S8 ¦ RALF23 does not modulate constitutive association between FER and LRX4.

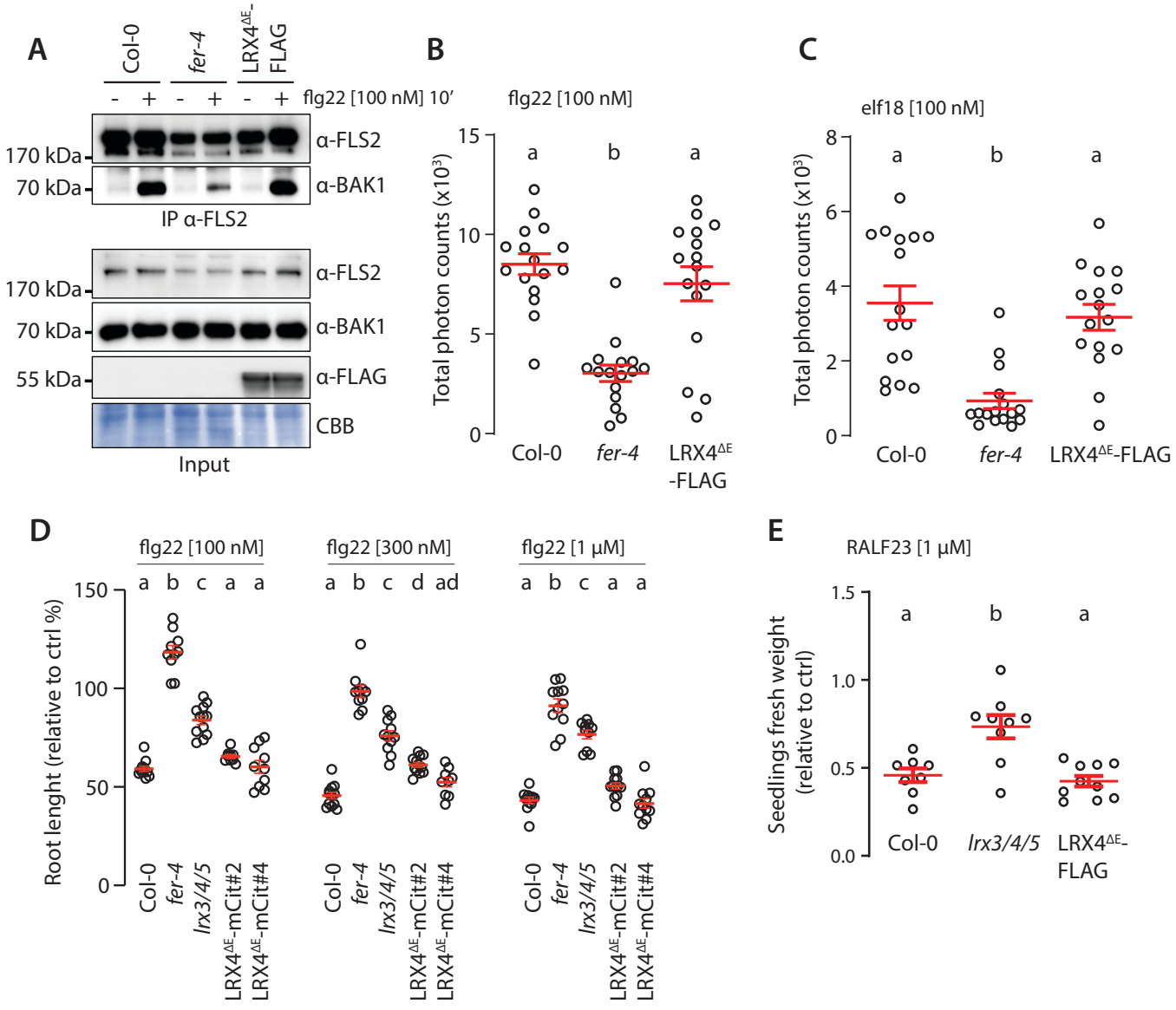

Fig. S9 ¦ Overexpression of LRX4ΔE does not affect PTI.

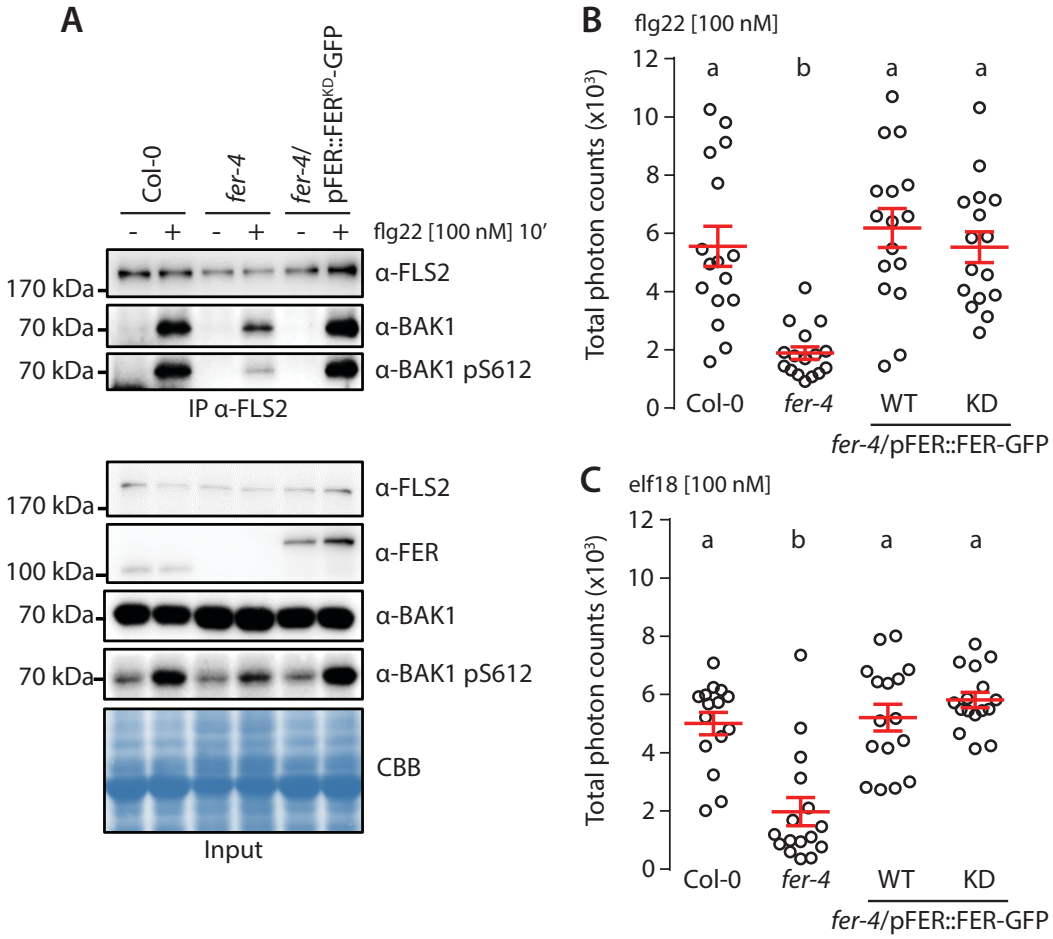

Fig. S10 ¦ FER kinase activity is dispensable to support PTI signaling.

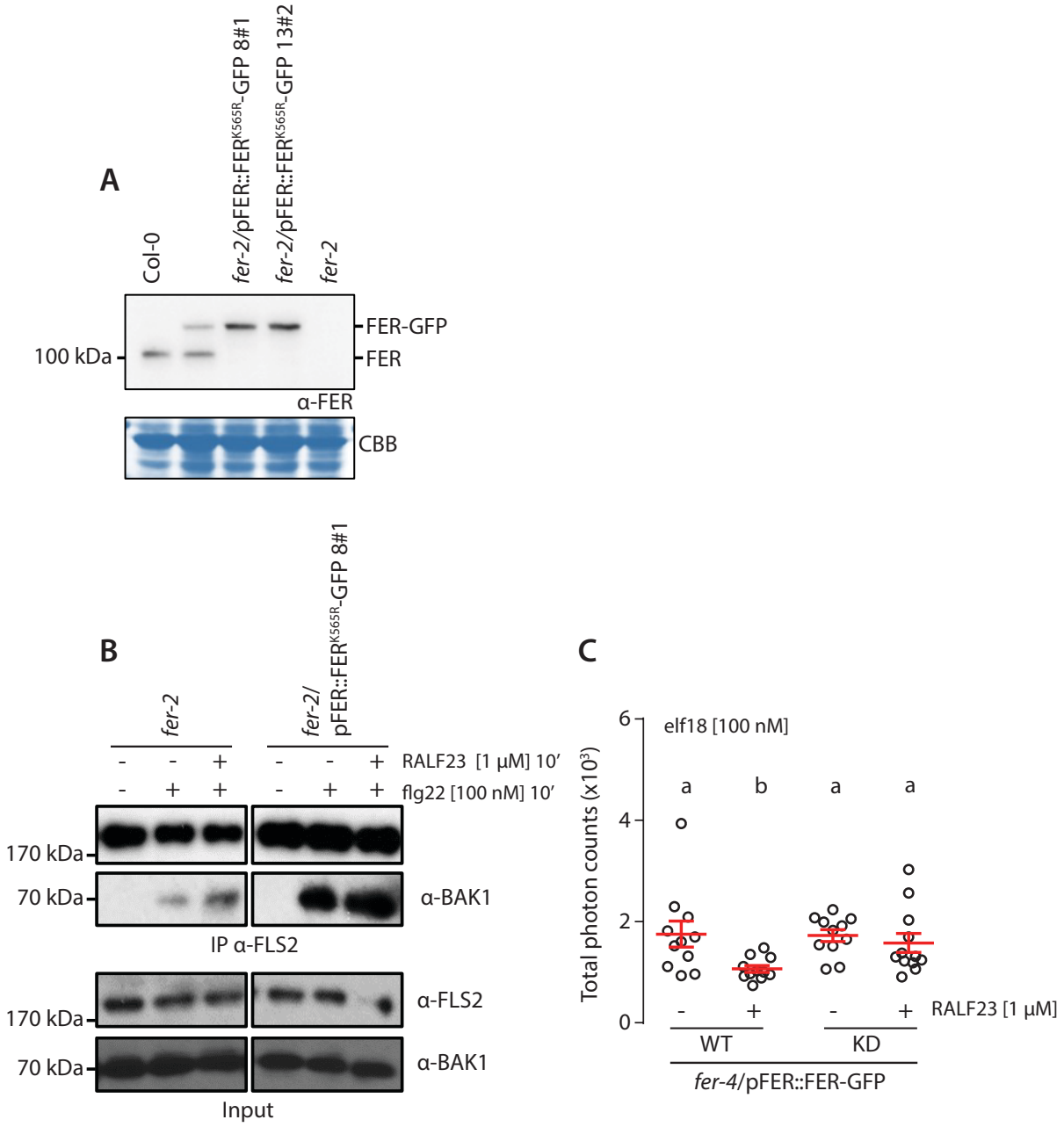

Fig. S11 ¦ Inhibition of PTI signaling by RALF23 requires FER kinase activity.

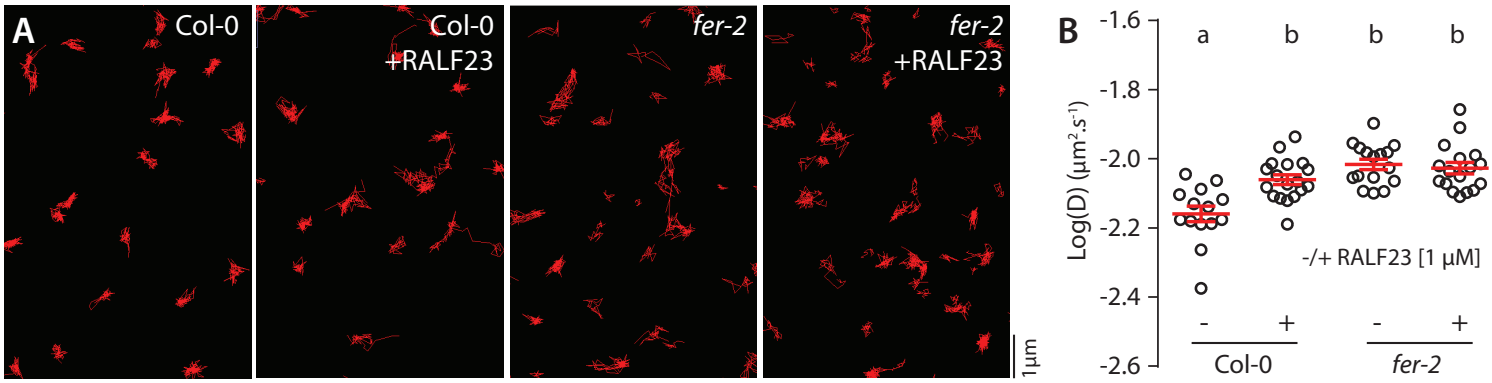

Fig. S12 ¦ Analysis of FLS2-GFP single particle dynamics upon RALF23 treatment.

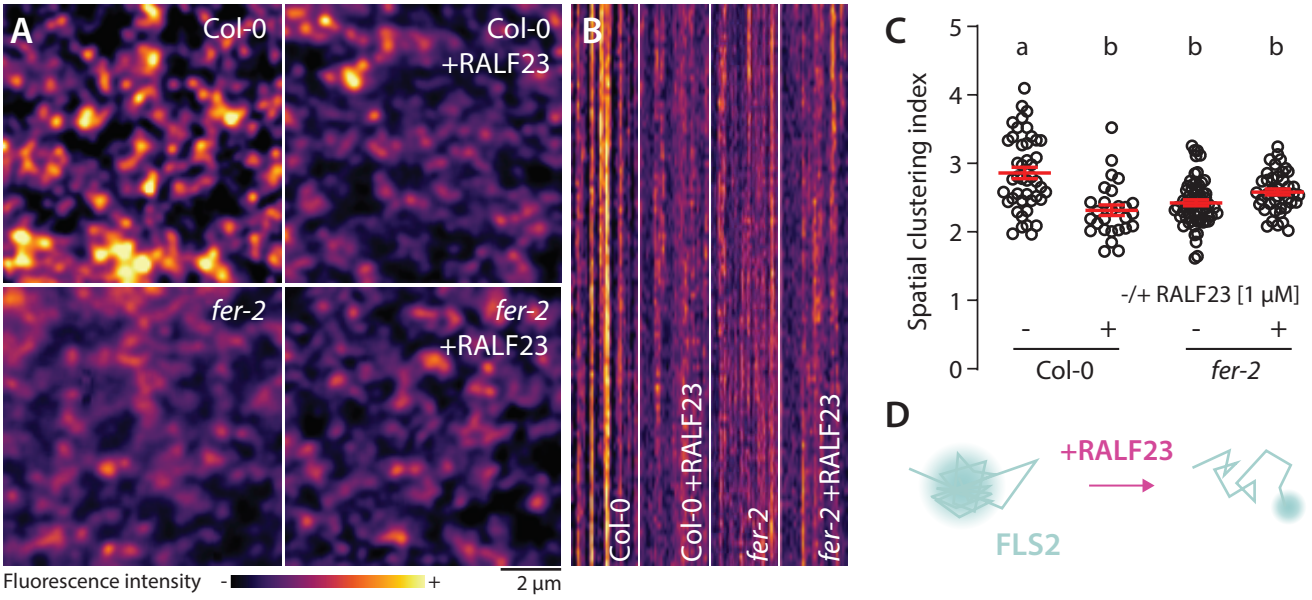

Fig. S13 ¦ Analysis of FLS2-GFP organization upon RALF23 treatment.

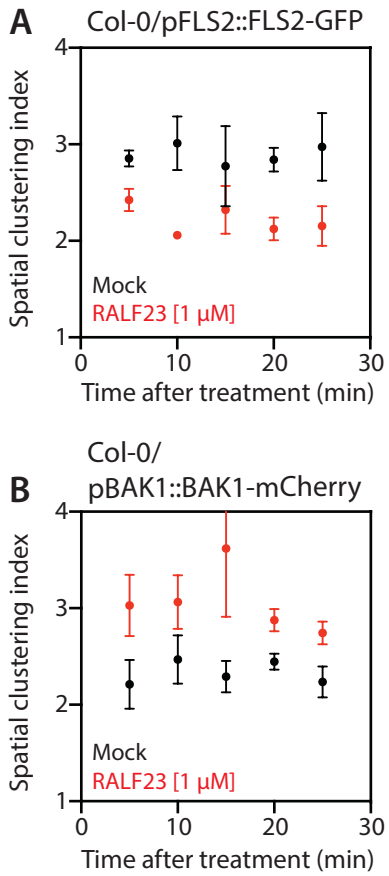

Fig. S14 ¦ Time-resolved analysis of the spatial clustering index.

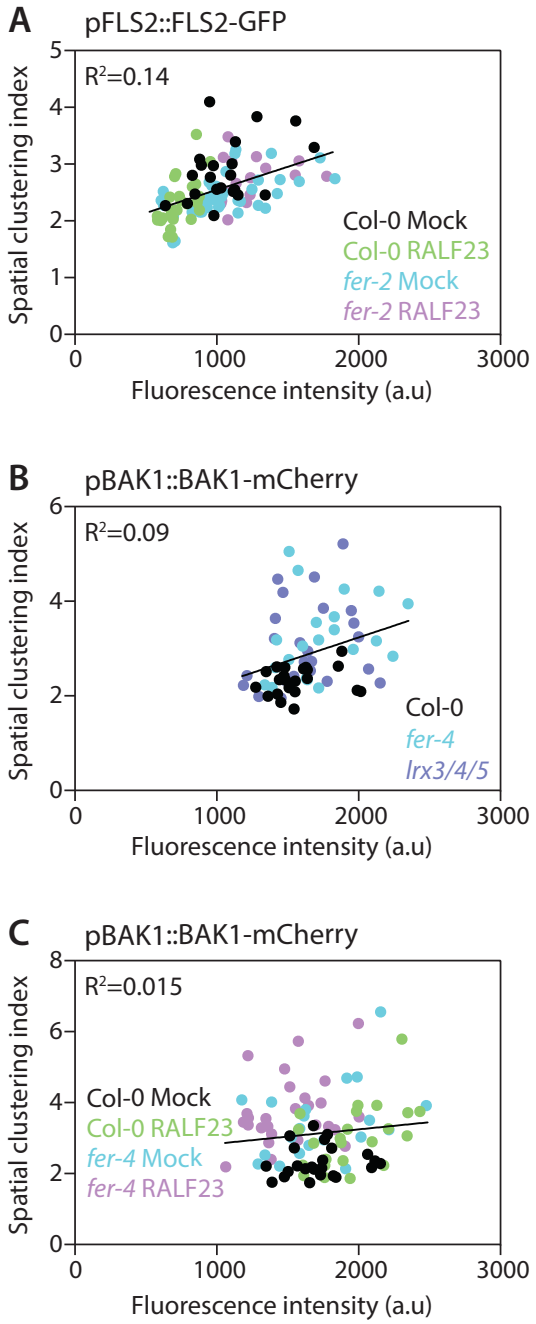

Fig. S15 ¦ Linear regression analysis of the relationship between the spatial clustering index and fluorescence intensity.